The Astrophysical Journal, 581:626–653, 2002 December 10

A *FAR ULTRAVIOLET SPECTROSCOPIC EXPLORER* SURVEY OF LATE-TYPE DWARF STARS

Seth Redfield,[1] Jeffrey L. Linsky,[2] Thomas B. Ake,[3] Thomas R. Ayres,[4] A. K. Dupree,[5] Richard D. Robinson,[3] Brian E. Wood,[1] and Peter R. Young[5,6]

Received 2002 May 15; accepted 2002 August 12

ABSTRACT

We describe the 910–1180 Å spectra of seven late-type dwarf stars obtained with the *Far Ultraviolet Spectroscopic Explorer (FUSE)* satellite. The stars include Altair (A7 IV), Procyon (F5 IV–V), α Cen A (G2 V), AB Dor (K1 V), α Cen B (K2 V), ϵ Eri (K2 V), and AU Mic (M0 V). We present line identifications, fluxes, Doppler shifts, and widths. Doppler shifts are measured with respect to heliocentric wavelength scales determined from interstellar absorption lines, and are compared with transition region line shifts seen in *Hubble Space Telescope* (*HST*) ultraviolet spectra. For the warmer stars the O VI lines extend the trend of increasing redshift with line formation temperature, but for the cooler stars the O VI line redshifts are essentially zero. The C III and O VI lines of most stars in the sample are best fit with two Gaussians, and we confirm the correlation of increasing importance of the broad component with increasing stellar activity. The nonthermal velocities of the narrow component are subsonic and exhibit a trend toward larger velocities with decreasing surface gravity, while the nonthermal velocities of the broad components show no obvious trend with stellar gravity. The C III and O VI lines of Altair show unique broad horned profiles. Two flares were observed on AU Mic. One shows increasing continuum flux to shorter wavelengths, which we interpret as free-free emission from hot plasma, and relatively narrow, redshifted C III and O VI emission. The other shows very broad line profiles.

Subject headings: stars: activity — stars: chromospheres — stars: late-type — techniques: spectroscopic — ultraviolet: stars

1. INTRODUCTION

The spectroscopically rich far-ultraviolet (FUV) between the Lyman continuum edge (912 Å) and about 1200 Å is relatively unexplored because MgF_2, the optical coating typically used in ultraviolet (UV) spectrographs, has rapidly decreasing reflectivity at wavelengths below 1200 Å. As a practical matter, the many MgF_2 overcoated optical surfaces used in the high-resolution modes of the *Hubble Space Telescope* (*HST*) spectrographs (Goddard High Resolution Spectrograph [GHRS] and the Space Telescope Imaging Spectrograph [STIS]) make it difficult to observe spectral features at wavelengths shortward of the C III multiplet at 1176 Å. The *Copernicus* and *Orbiting and Retrievable Far and Extreme Ultraviolet Spectrometer* (*ORFEUS*) missions with LiF or SiC optical surfaces obtained FUV spectra of a limited number of late-type stars because of the low sensitivity or short duration of these missions. The *Far Ultraviolet Spectroscopic Explorer* (*FUSE*) combines high throughput with LiF or SiC coated optics, and long mission duration to support deep exposures of many targets. For a description of *FUSE* and its capabilities, see Moos et al. (2000) and Sahnow et al. (2000).

The present paper is part of a series presenting *FUSE* observations of a representative sample of late-type stars. Here we consider main-sequence stars ranging in spectral type from A7 V (Altair) to M0 V (AU Mic). Table 1 summarizes the properties of the seven dwarfs. Preliminary discussions of the *FUSE* observations of AB Dor, and four of the other dwarfs (α Cen A, α Cen B, ϵ Eri, and AU Mic), were presented by Ake et al. (2000, 2001). Here we take a closer look at the *FUSE* spectra of the seven stars and show trends with spectral type and activity as measured by the X-ray surface flux (F_X). The *ORFEUS* spectrograph (Hurwitz et al. 1998) obtained spectra in the 912–1218 Å wavelength band of Procyon, α Cen A, α Cen B, AB Dor, and ϵ Eri with a resolution of $\sim$95 km s^{-1}. To our knowledge, only the AB Dor data set has been published (Schmitt et al. 1997; Schmitt, Cutispoto, & Krautter 1998). *Copernicus* observed selected wavelength regions in the FUV with high spectral resolution for Altair, Procyon, α Cen A, and ϵ Eri, including the O VI line near 1032 Å and in some cases the C III 977 Å line, C III 1176 Å multiplet, and H I Lyβ. Aside from a weak detection of O VI 1032 Å presented by Evans, Jordan, & Wilson (1975), these observations have not been published, probably because of the generally low signal-to-noise ratio (S/N). Thus, the *FUSE* observations with $c\Delta\lambda/\lambda \sim 15$ km s^{-1} resolution and high S/N open a new window on the atmospheres of late-type dwarf stars.

2. *FUSE* OBSERVATIONS

Table 2 summarizes the observations of the seven late-type dwarfs obtained as part of two *FUSE* Science Team programs: The "cool stars spectral survey" and "local ISM D/H" programs. All targets except Altair were observed in time-tagged mode. Altair is a bright source with significant continuum emission. Given its significantly higher count rate than the other sources, it was recorded in

[1] JILA, University of Colorado, Boulder, CO 80309-0440; sredfiel@casa.colorado.edu.
[2] JILA, University of Colorado; and NIST, Boulder, CO 80309-0440.
[3] Johns Hopkins University, Baltimore, MD 21218.
[4] CASA, University of Colorado, Boulder, CO 80309.
[5] Harvard-Smithsonian Center for Astrophysics, Cambridge, MA 02138.
[6] Space Science and Technology Department, Rutherford Appleton Laboratory, Chilton, Didcot, Oxfordshire, OX11 0QX, UK.

TABLE 1
PROPERTIES OF *FUSE* DWARF STARS

Star Name	HD No.	Spectral Type	v_{rad} (km s^{-1})	m_V	$B-V$	log F_X[a] (ergs cm^{-2} s^{-1})	$v \sin i$[b] (km s^{-1})	v_{LISM}[c] (km s^{-1})	Distance[d] (pc)
Altair	187642	A7 V	−26.1	0.77	0.22	3.86	210	−17.9, −21.5, −25.3	5.15
Procyon	61421	F5 IV–V	−3.2	0.34	0.40	4.85	5.0	20.2, 22.9	3.50
α Cen A.....	128620	G2 V	−24.6	−0.01	0.71	4.37	3	−18.0	1.35
AB Dor	36705	K1 V	29.2	6.93	0.80	7.89	91	5.2, 14.5, 19.6	14.9
α Cen B.....	128621	K2 V	−20.7	1.33	0.88	4.71	2	−18.0	1.35
ϵ Eri	22049	K2 V	15.5	3.73	0.88	5.74	2.0	20.9	3.22
AU Mic.....	197481	M0 V	1.2	8.61	1.44	7.44	<6.2	−21.2	9.94
Sun.....	...	G2 V	0.0	−26.74	0.65	4.51	2.2	...	4.8×10^{-6}

[a] Soft X-ray surface fluxes (0.1–2.4 keV) obtained with the *ROSAT* satellite (Hünsch et al. 1999).
[b] Values for $v \sin i$ were taken from van Belle et al. 2001 for Altair, Hale 1994 for Procyon, Pallavicini et al. 1981 for α Cen A, Smith, Edvardsson, & Frisk 1986 for α Cen B, Brandt et al. 2001 for AB Dor, Fekel 1997 for ϵ Eri, Pettersen 1980 for AU Mic, and Smith 1978 for the Sun.
[c] Heliocentric interstellar radial velocities taken from Lallement et al. 1995 for Altair, Linsky et al. 1995 for Procyon, Linsky & Wood 1996 for α Cen A and B, Dring et al. 1997 for ϵ Eri, and Redfield & Linsky 2002b for AU Mic.
[d] *Hipparcos* parallaxes taken from the SIMBAD database.

histogram mode. All targets were observed through the medium-resolution slit (MDRS, $4\farcs0 \times 20'$) or large aperture (LWRS, $30' \times 30'$). The LWRS has the advantage of usually including light from all of the LiF and SiC channels inside the large aperture for the duration of the exposure, frequently at the expense of high airglow contamination, especially at Lyβ and Lyγ but also in many O I and N I lines. The MDRS reduces airglow contamination, but thermal effects often cause one or more of the channels to drift out of the MDRS aperture during an exposure, because only the LiF1 channel is used for guiding. The local ISM D/H program used the MDRS aperture to minimize airglow contamination, especially in the Lyβ line. As a result, observations of Procyon, α Cen A, α Cen B, and ϵ Eri typically have low S/N in the short-wavelength portions of their spectra not included in the LiF1 channel (987–1188 Å). The other stars were observed through the LWRS aperture to maximize the probability of recording signal from all channels.

The spectral images were processed with CalFUSE 2.0.5.[7] This version of the pipeline provides a more accurate wavelength scale, removes large noise event bursts, corrects for misplaced photons at low-sensitivity portions of the detector (so-called "walk" problem), improves corrections for scattered light and astigmatism, extracts the spectrum using an "optimal" algorithm, and applies a more accurate flux calibration (flux errors are <15%; Oegerle, Murphy, & Kriss 2000).[8] Individual exposures were reduced separately, and the integrated flux in strong emission lines was used to test the consistency of the signal recorded in each segment, throughout the entire observation. Exposures for each segment were cross-correlated and co-added, removing those with significant drops in signal, due to the target drifting out of the aperture (a common occurrence for MDRS observations). Redundant segments were not co-added because the spectral resolution would be severely degraded. Therefore, only segments with the highest effective area (i.e., highest S/N) are used to assemble the complete spectrum from 900 to 1200 Å. The correction for astigmatism (spectral line curvature perpendicular to the dispersion) improves the spectral resolution by 5%–10% compared with earlier versions of CalFUSE used to reduce the previously published spectra of the cool stars AB Dor (Ake et al. 2000) and Capella (Young et al. 2001).

The relative wavelength scale within a given detector channel is accurate to ± 5 km s^{-1} over most of the FUV bandpass, except for some deterioration at the far edges of the individual channels (Dixon 2001).[9] Because of the lack

[7] See http://fuse.pha.jhu.edu/analysis/analysis.html.

[8] *FUSE* Data Handbook Version 1.1 is available at: http://fuse.pha.jhu.edu/analysis/dhbook.html.
[9] Introduction to CalFUSE version 2.0 is available at: http://fuse.pha.jhu.edu/analysis/calfuse_intro.html.

TABLE 2
SUMMARY OF *FUSE* OBSERVATIONS

Star Name	Data Set	Observation Date	Aperture	Number of Exposures	Exposure Time (ks)
Altair	P1180701	2001 Sep 14	LWRS	8	4.2
Procyon	P1041801	2001 Oct 21	MDRS	7	5.3
α Cen A.....	P1042601	2001 Jun 25	MDRS	8	15.3
AB Dor	X0250201	1999 Oct 20	LWRS	1	22.1
AB Dor	X0250203	1999 Dec 14	LWRS	6	24.2
α Cen B.....	P1042501	2001 Jun 24	MDRS	13	22.7
ϵ Eri	P1040701	2000 Dec 8	MDRS	15	34.8
AU Mic.....	P1180801	2000 Aug 26	LWRS	9	17.3
AU Mic.....	P2180401	2001 Oct 10	LWRS	13	26.5

of an on-board wavelength calibration lamp, we established the zero point of the wavelength scale according to interstellar absorption features in the C II 1036.3 Å and C III 977.0 Å lines, and by comparing the C III 1176 Å lines in *FUSE* with wavelength-calibrated observations by *HST*. The procedure is described in the Appendix.

3. SPECTRAL LINE IDENTIFICATION

Figures 1 and 2 illustrate *FUSE* spectra of the seven stars in two bandpasses, 900–1050 Å and 1050–1200 Å, and the average quiet-Sun spectrum obtained with the Solar Ultraviolet Measurements of Emitted Radiation (SUMER) instrument on the *Solar and Heliospheric Observatory* (*SOHO*; Curdt et al. 2001). The spectral resolution of SUMER is about 80 mÅ, corresponding to 24 km s^{-1} at 1000 Å, and the accuracy of the velocity scale is $\sim$3 km s^{-1} using chromospheric lines as velocity fiducials in the absence of an on-board wavelength-calibration lamp. Our line list is based on the solar spectrum (Feldman & Doschek 1991; Curdt et al. 1997) and the CHIANTI version 3.03 spectral database (Dere et al. 1997, 2001). The spectra of the seven dwarf stars include a rich collection of lines formed at 5×10^4 to 5×10^5 K and many lower temperature chromospheric emission lines, especially H I and C I. Figure 3 graphically demonstrates the abundance and diversity of stellar emission lines detected in the UV. Features detected in *HST* spectra were taken from line lists based on observations of AU Mic (Pagano et al. 2000) and α Cen A (I. Pagano, in preparation). Many important lines are observable only by *FUSE*, including N II, N III, O VI, Ne V, S VI, and the coronal forbidden lines, Fe XVIII and Fe XIX.

Table 3 lists the observed emission lines in each stellar spectrum, rest wavelengths, and integrated line fluxes. Local continua were calculated from line-free regions directly adjacent to the emission feature. Only relatively strong, isolated lines were included in Table 3. When a strong line was positively identified, all members of the multiplet were included, regardless of strength or degree of blending with other lines. On the other hand, the relatively weak, and highly blended C I multiplets from 1110 to 1160 Å are not included in Table 3, although some are seen in Figure 2. Lines that are blended in all seven stars were grouped together. Blends in isolated stars are indicated by footnotes. When a target spectral line was not detected, we provide a conservative upper limit of the integrated flux.

Lyman series lines beyond Lyβ are not included in Table 3, although in some cases we detected stellar emission in these lines. Unfortunately, these lines are severely contaminated by H I and O I airglow (Feldman et al. 2001). In order to quantify the terrestrial contamination, we compared the full data set with a nighttime-only data set. At night, the airglow is significantly reduced, but the stellar emission should remain the same, albeit with a lower S/N due to the shorter integration time. As mentioned in § 2, the aperture size also influences the level of airglow contamination. Figure 4 depicts the Lyα line from *HST*, together with the Lyβ line from *FUSE*, for the four stars in our sample that were observed with the MDRS aperture (see Table 2). The *FUSE* spectra include the full data set and nighttime only. The shaded region indicates where the former exceeds the latter, presumably owing to additional terrestrial airglow contamination. All demonstrate that the Lyβ airglow does not dominate the Lyβ stellar emission, and except for Procyon, the agreement between the full and nighttime-only spectra is very good. Figure 5 shows the same comparison, but for the remaining three targets observed in the LWRS aperture, including the solar comparison based on the SUMER spectral atlas. H I airglow dominates the Lyβ spectra of these stars. However, given that these are the most rapidly rotating stars in our sample, there does appear to be stellar Lyβ emission beyond the central airglow emission. Altair was observed in histogram mode, and unfortunately we cannot separate daytime from nighttime photons.

There is no clear evidence for local interstellar medium (LISM) deuterium absorption against the Lyβ emission line, as there is for Lyα. Given the factor of 5.3 decrease in optical depth from D I 1215.3 Å to D I 1025.4 Å and the low H I column densities to nearby targets, the detection of D I absorption against the Lyβ emission would require much higher S/N and higher spectral resolution than is available in the present data. The velocity of interstellar D I absorption is indicated in Figures 4 and 5 by the vertical dashed line.

We call attention to the Fe XVIII 974.86 Å and Fe XIX 1118.06 Å lines seen in the spectra of the most active dwarfs in our sample (AB Dor, AU Mic, and ϵ Eri). These features, formed in stellar coronae at $T \sim 10^7$ K, are present in solar flares and were predicted to occur in *FUSE* spectra of active stars by Feldman & Doschek (1991). Young et al. (2001) identified Fe XVIII in the *FUSE* spectrum of Capella. Properties of these features and a search for other coronal lines in *FUSE* spectra will be presented in a companion paper (Redfield et al. 2002a).

The spectra of α Cen A, α Cen B, ϵ Eri, and AU Mic contain the H_2 1–4 $Q(3)$ emission line at 1163.9 Å, which is a fluorescent Werner band line pumped by O VI 1031.8 Å from the $v'' = 1$, $J'' = 3$ level in the ground electronic state to the $v' = 1$, $J' = 3$ level in the C electronic state. The 1163.9 Å line is expected to be the brightest in this fluorescent progression, since it has the highest branching ratio. The 1163.9 Å line also appears in *FUSE* spectra of T Tau as reported by Wilkinson et al. (2002), who describe the fluorescence process in more detail. The 1119.075 Å line is predicted to be the next brightest line in the fluorescent progression. It is detected as a very weak feature in AU Mic (see Fig. 2), and is perhaps seen in ϵ Eri, but is absent in α Cen A and B. In late-type giants, an unidentified feature at 1118.86 Å is detected. Because observations of this spectral region in giant stars detect numerous fluorescent Fe II lines (Harper et al. 2001), it is possible that the feature at 1118.86 Å is Fe II. However, in the *FUSE* dwarf star spectra, there are no other Fe II lines, and therefore we identify this feature as H_2 instead of Fe II. We searched archival STIS spectra for the third brightest line in the progression, at 1208.932 Å, but could not definitely detect it in echelle spectra of AU Mic or ϵ Eri. We believe that H_2 is present in the cooler portions of the chromospheres of these four stars, but deeper observations are needed to understand the fluorescent processes in more detail.

All these stars have very similar spectra. Figure 6 shows the correlation between spectral type ($B-V$) and the flux ratio of two of the strongest lines in this spectral range, C III 977 Å and O VI 1032 Å. Solar values have been added for "quiet Sun" and "active region" observations recorded by SUMER (Curdt et al. 2001). The quiet-Sun value fits in well with the stellar observations. The active region flux ratio is

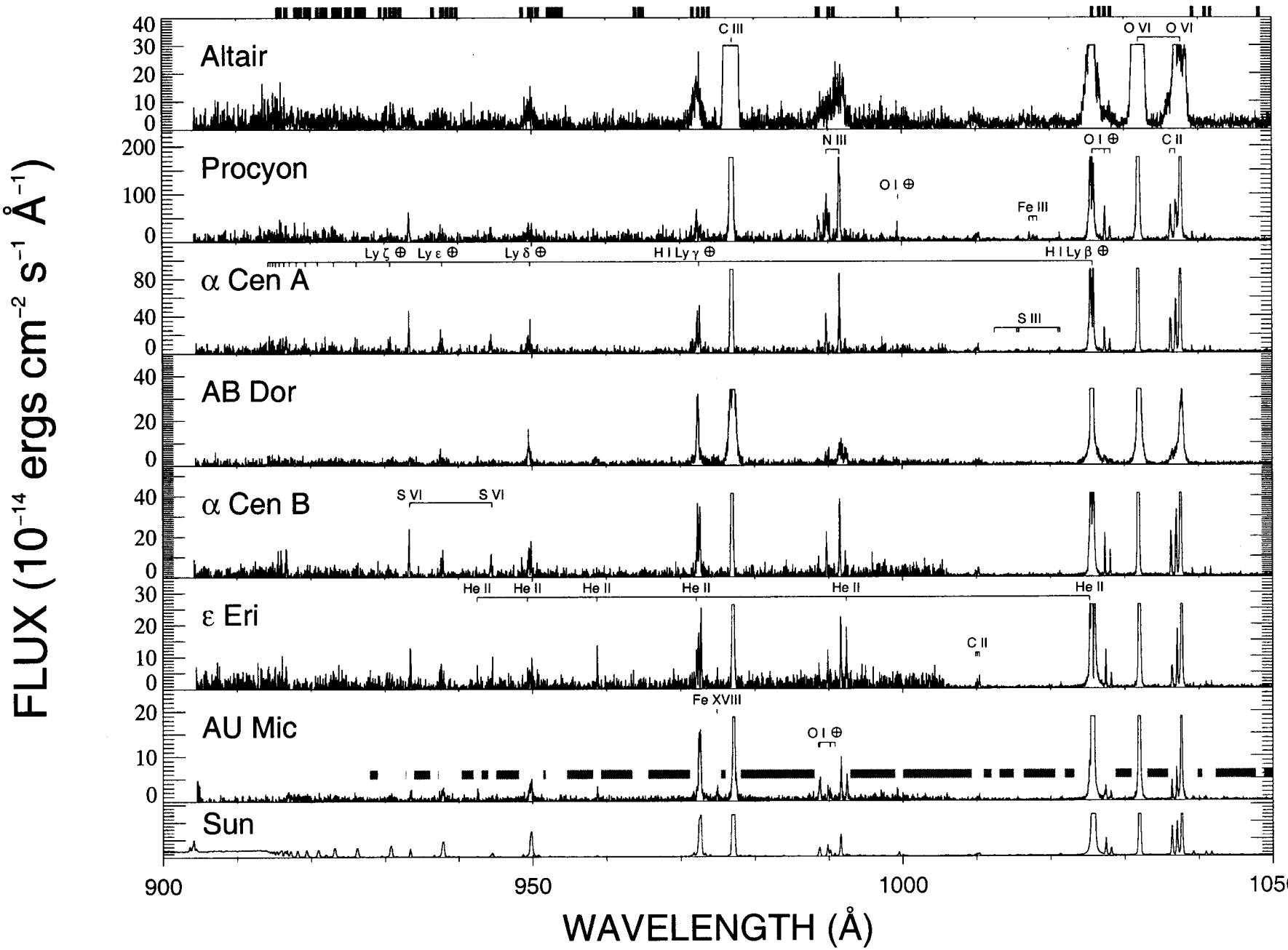

FIG. 1.—*FUSE* spectra of dwarf stars and the *SOHO*/SUMER spectrum of the average quiet Sun (scaled relative to the stars) in the 900–1050 Å bandpass. Important emission lines are labeled. Locations of airglow emission are indicated by grey bands at the top of the figure. Shaded bands in the AU Mic panel represent "line-free" spectral windows, used to calculate the continuum discussed in § 8. Terrestrial airglow contaminations are indicated by circled crosses.

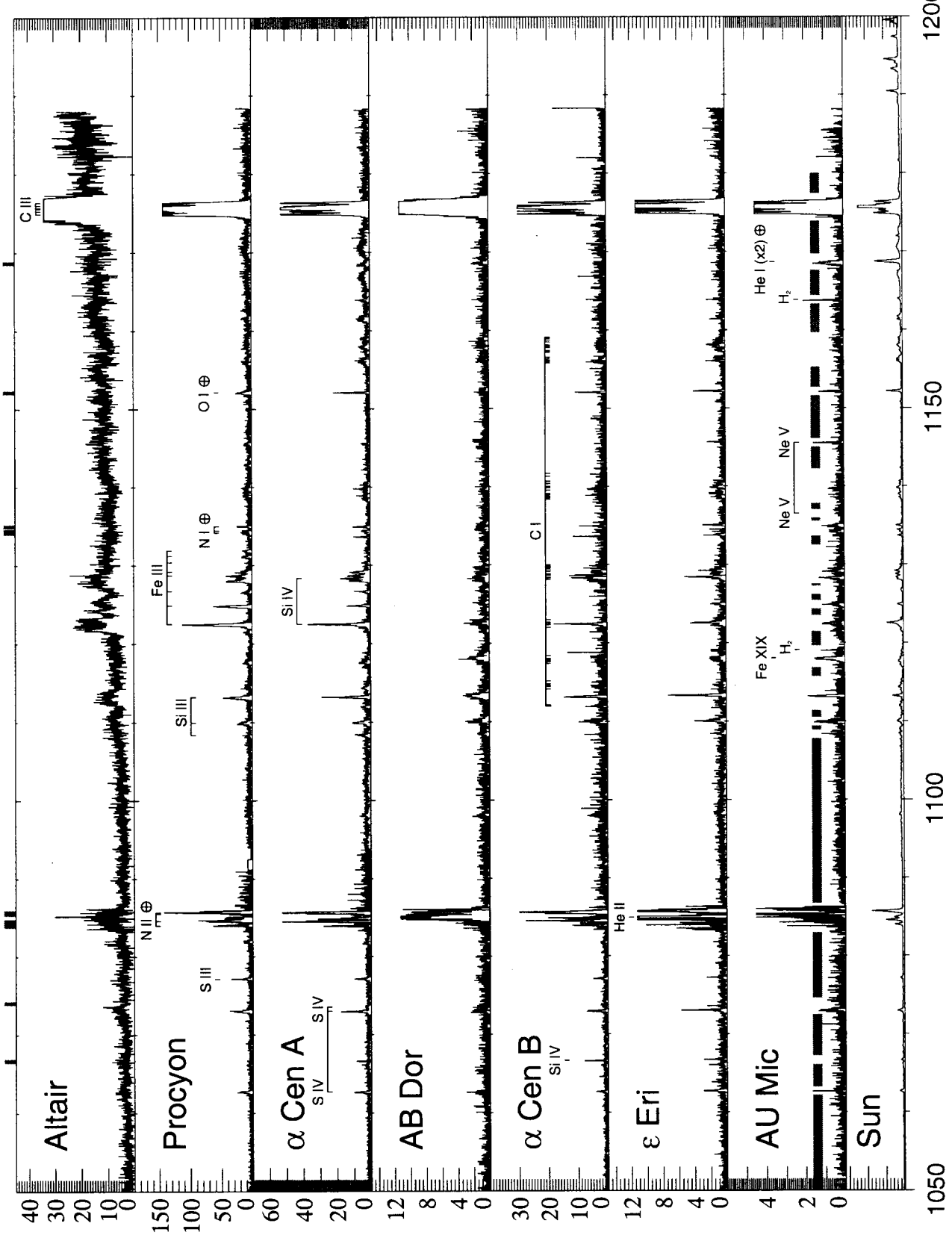

FIG. 2.—Same as Fig. 1, but for 1050–1200 Å

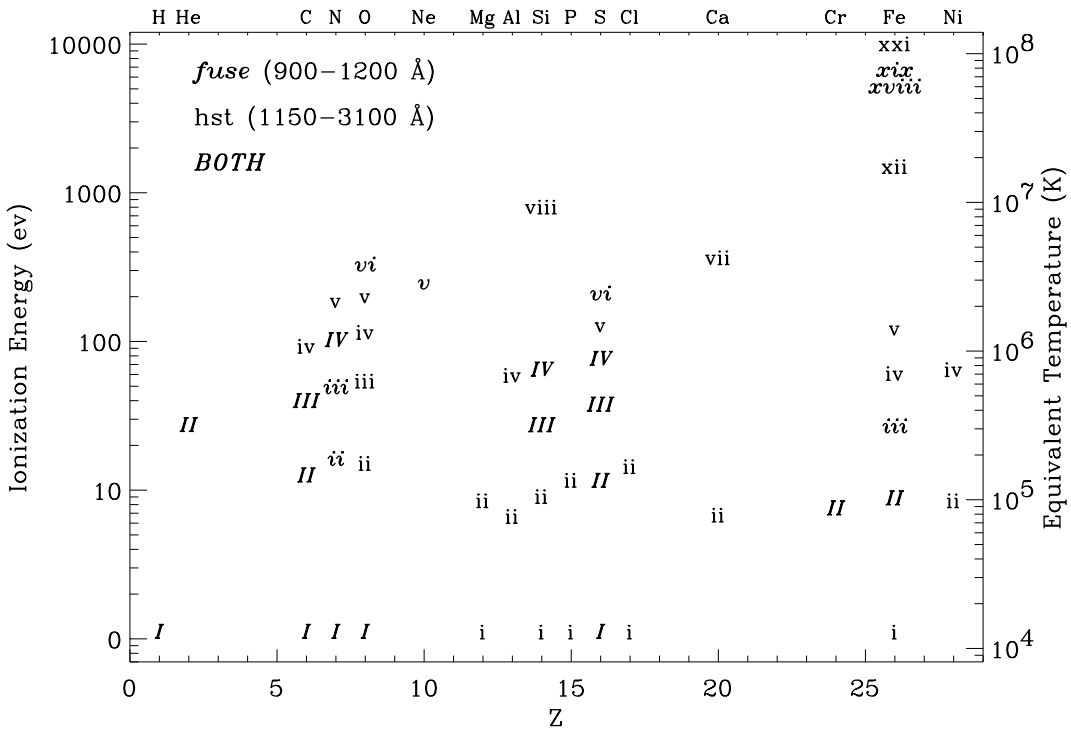

FIG. 3.—Inventory of stellar UV emission lines detected by *FUSE* (*lowercase italics*), by *HST* (*lowercase roman*), and by both satellites (*uppercase italics*). Ionization energy (eV) and equivalent temperature (K) are plotted against atomic number, with the elements identified along the top axis.

significantly smaller, but it illustrates the cause for the decrease in the flux ratio toward cooler stars (larger values of $B-V$). Stellar convection zone thickness increases toward the coolest stars. Convection powers dynamos that manifest into active regions on the stellar surface, where energy is dissipated through magnetic reconnection. Since these highly energetic events produce a larger amount of high-temperature plasma than less energetic heating processes, one expects that the higher temperature lines, like O VI, will be relatively brighter than the lower temperature lines, like C III, in the cooler and more active stars.

The Sun and our seven dwarfs display many of the same fundamental characteristics. The incredible similarity of the spectra in Figures 1 and 2 reinforce this fact. Our observations of other solar-like stars not only allow for a context of well-studied solar phenomena, but also provide a means of comparing these properties as a function of stellar parameters, as shown in Figure 6. In the next three sections (§§ 4–6) we continue to discuss fundamental spectral diagnostics and compare the stars in our sample to each other and to the Sun. In §§ 7 and 8, we present unique properties observed in the *FUSE* spectrum of two individual stars (Altair and AU Mic).

4. LINE FLUXES

We extracted fluxes for C III 977 Å, O VI 1032 Å, and C III 1176 Å from the *ORFEUS* data archive for comparison with the *FUSE* line strengths. The *ORFEUS* fluxes are listed in Table 4. The *FUSE* data have higher S/N, better absolute fluxes (at least through the LWRS), higher spectral resolution to better separate the emission lines from an underlying continuum or line blends, and a better absolute wavelength scale (after cross-calibration, as discussed in the Appendix). We could measure all three features in the *ORFEUS* spectra of Procyon and AB Dor, but only C III 977 Å and O VI 1032 Å in α Cen A, α Cen B, and ϵ Eri. Listed in parentheses alongside each flux value in Table 4 is the difference between the *ORFEUS* and *FUSE* flux. To our surprise, the best agreement was for the star that likely is the most variable: AB Dor. For this star the *ORFEUS* fluxes ranged from -1% to $+7\%$ compared to the *FUSE* fluxes. We have not used the *ORFEUS I* C III 977 Å flux (-37%) but rather the deeper reobservation taken with *ORFEUS II*, in which the C III 977 Å flux agrees very well with our *FUSE* observations ($+7\%$). For α Cen B the corresponding range is -16% to $+52\%$, and for ϵ Eri the range is -19% to $+12\%$. The two stars that we would expect to show the least time variability are Procyon and α Cen A. For Procyon the range is $+20\%$ to $+38\%$, while for α Cen A the range is -14% to $+9\%$.

What is the most likely explanation for the large flux differences between the *ORFEUS* and the *FUSE* data? Although active stars exhibit short-term variability caused by flaring and rotation of active regions onto and off of the disk, inactive stars can also show long-term variability due to activity cycles. However, we feel the most likely explanation for the flux differences is instrumental. An important clue is the comparison between the *HST* (STIS or GHRS) and *FUSE* fluxes for the C III 1176 Å multiplet. Table 5 includes in the right-hand column the differences between the *HST* and *FUSE* fluxes for this line. The best agreements are for Altair, AU Mic, and AB Dor, all of which were observed through the LWRS, whereas the worst agreements are for α Cen A and ϵ Eri, observed through the MDRS. Thus, the most likely explanation for the flux difference is loss of light as a star drifts to the edge of the MDRS

TABLE 3

OBSERVED EMISSION LINE FLUXES

LINE	λ_{rest} (Å)	INTEGRATED FLUX (10^{-14} erg cm^{-2} s^{-1})						
		α Aql	Procyon	α Cen A	AB Dor	α Cen B	ϵ Eri	AU Mic[a]
S VI	933.38	4.8 ± 0.9	10.8 ± 1.3	5.4 ± 1.1	1.9 ± 0.3	3.2 ± 0.3	2.1 ± 0.2	0.5 ± 0.1
He II	942.49	<1.9	<3.9	<1.0	0.8 ± 0.2	<0.4	0.6 ± 0.1	0.3 ± 0.1
S VI	944.52	<3.3	7.2 ± 1.0	4.1 ± 0.9	<1.2	2.1 ± 0.2	0.8 ± 0.1	<0.4
He II	958.70	<2.2	<3.2	<1.4	1.3 ± 0.3	<0.3	1.4 ± 0.1	0.5 ± 0.1
Fe XVIII	974.86	<2.3	<3.2	<0.6	<3.1	<0.6	0.9 ± 0.1	0.6 ± 0.2
C III	977.02	272 ± 27	543 ± 54	224 ± 22	$52.6^{b} \pm 5.3$	93.8 ± 14.2	40.4 ± 4.0	15.3 ± 1.5
N III	989.80		33.7 ± 3.4	8.0 ± 1.4	2.0 ± 0.3	3.2 ± 0.3	1.7 ± 0.2	1.2 ± 0.1
	991.51, 991.58	29.1 ± 2.9^{c}	56.3 ± 5.6^{d}	15.8 ± 2.1^{d}	5.0 ± 0.5^{d}	6.5 ± 0.7^{d}	3.8 ± 0.4^{d}	1.7 ± 0.2^{d}
He II	992.36	$<5.6^{e}$	<5.5	1.7 ± 0.6	1.9 ± 0.3^{e}	1.4 ± 0.2	2.5 ± 0.3	1.3 ± 0.2
C II	1009.86, 1010.08, 1010.37	6.6 ± 0.7	8.9 ± 0.9	3.3 ± 0.3	1.1 ± 0.2	1.4 ± 0.2	0.9 ± 0.1	0.3 ± 0.1
S III	1012.5	<2.5	<4.2	0.5 ± 0.2	<0.4	0.3 ± 0.1	<0.5	<0.2
	1015.57, 1015.78	<3.6	2.6 ± 0.4	1.0 ± 0.2	<0.7	0.6 ± 0.1	0.2 ± 0.1	0.3 ± 0.1
Fe III	1017.25		2.8 ± 0.4	0.6 ± 0.1	<0.7	0.3 ± 0.1	<0.3	<0.2
	1017.75	$<7.9^{f}$	2.0 ± 0.3	0.5 ± 0.1	<0.5	0.3 ± 0.1	<0.4	<0.2
	1018.29		2.1 ± 0.3	0.3 ± 0.1	<0.3	<0.7	<0.5	<0.3
S III	1021.11, 1021.34	<5.4	2.6 ± 0.3	1.5 ± 0.2	1.0 ± 0.1	0.9 ± 0.1	0.3 ± 0.1	0.4 ± 0.2
O VI	1031.93	82.1 ± 8.2	223 ± 49	95.4 ± 9.5	44.9 ± 4.5	61.6 ± 11.5	43.3 ± 4.3	20.9 ± 2.4
C II	1036.34[b]	$<5.7^{g}$	16.4 ± 1.6	8.1 ± 0.8	$<4.9^{g}$	4.1 ± 0.2	1.5 ± 0.2	0.7 ± 0.1
C II	1037.02		22.8 ± 2.3^{g}	12.2 ± 1.2		6.1 ± 0.3	3.1 ± 0.3	1.3 ± 0.1
O VI	1037.62	$<53.4^{g}$	111 ± 11^{g}	45.7 ± 4.6	$<25.4^{g}$	29.6 ± 3.0	22.9 ± 2.3	10.6 ± 1.1
S IV	1062.68	<7.5	5.5 ± 0.6	1.3 ± 0.2	0.7 ± 0.1	0.6 ± 0.1	0.4 ± 0.1	0.2 ± 0.1
Si IV	1066.61, 1066.64, 1066.65	<6.6	<6.4	0.7 ± 0.2	<0.5	0.7 ± 0.1	0.2 ± 0.1	<0.2
S IV	1073.00	$<3.1^{h}$	8.0 ± 0.8	2.7 ± 0.3	1.1 ± 0.2^{h}	1.1 ± 0.1	0.6 ± 0.1	0.4 ± 0.1
	1073.53		<3.2	<1.7		<1.3	0.1 ± 0.1	<0.2
S III	1077.13	<8.6	4.9 ± 0.6	1.3 ± 0.2	<0.9	0.9 ± 0.1	0.2 ± 0.1	<0.2
N II	1083.99	$<16.5^{i}$	8.9 ± 1.4	3.0 ± 1.0	12.4 ± 1.2^{i}	1.7 ± 0.3	0.7 ± 0.1	<0.8
	1084.57, 1084.58		19.1 ± 2.0^{j}	7.9 ± 1.7^{j}		3.9 ± 0.4^{j}	1.7 ± 0.3^{j}	$<1.1^{j}$
He II	1084.94		5.7 ± 1.1^{k}	3.9 ± 1.1		2.7 ± 0.3	6.7 ± 0.7	1.5 ± 0.3
N II	1085.53, 1085.55, 1085.71		31.0 ± 3.1^{l}	16.7 ± 2.7^{l}		8.5 ± 0.9^{l}	4.3 ± 0.4^{l}	1.0 ± 0.2^{l}
Si III	1108.36	<10.1	<11.0	1.7 ± 0.3	1.1 ± 0.2	0.6 ± 0.1	0.3 ± 0.1	0.2 ± 0.1
	1109.94, 1109.97	<10.3	8.1 ± 0.8	3.1 ± 0.3	1.2 ± 0.2	2.0 ± 0.2	0.9 ± 0.1	0.5 ± 0.1
	1113.17, 1113.20, 1113.23	5.7 ± 1.0	12.3 ± 1.2	4.9 ± 0.5	2.0 ± 0.2	3.0 ± 0.3	1.2 ± 0.1	0.4 ± 0.1
Fe XIX	1118.06	< 8.6	< 9.4	< 4.3	1.8 ± 0.3	< 2.3	0.8 ± 0.1	0.7 ± 0.1
Si IV, Fe III	1122.49, 1122.53	16.3 ± 1.6	31.0 ± 3.1	7.7 ± 0.8	0.9 ± 0.2	3.2 ± 0.3	0.8 ± 0.1	0.4 ± 0.1
Fe III	1124.88	4.7 ± 0.9	14.4 ± 1.4	2.0 ± 0.3	<1.2	0.5 ± 0.1	0.3 ± 0.1	0.2 ± 0.1
	1126.73	<14.6	3.1 ± 0.5	0.9 ± 0.2	<1.0	0.9 ± 0.1	<0.7	<0.2
Fe III, Si IV, Si IV ..	1128.05, 1128.33, 1128.34	11.9 ± 1.2^{m}	30.4 ± 3.0^{m}	5.6 ± 0.6	1.0 ± 0.1^{m}	2.6 ± 0.3	0.8 ± 0.1	0.3 ± 0.1
Fe III	1128.72			2.5 ± 0.3		1.3 ± 0.1	<0.5	0.1 ± 0.1
	1129.19			2.9 ± 0.3		<3.0	0.3 ± 0.1	0.2 ± 0.1
	1130.40	<18.0	1.4 ± 0.4	1.1 ± 0.2	<0.9	<1.8	<1.0	<0.2
	1131.20	<19.8	3.6 ± 0.5	0.6 ± 0.2	<0.6	<0.9	<0.5	<0.2
	1131.92	<13.3	3.4 ± 0.5	<2.9	<0.9	<1.0	<0.5	<0.2
Ne V	1136.49	<10.0	<4.0	<1.9	<0.8	<1.1	<0.5	<0.2
	1145.58	<23.3	3.0 ± 0.6	0.3 ± 0.1	<1.0	<1.2	0.1 ± 0.1	0.2 ± 0.1
H_2	1163.85	<16.4	<7.1	1.1 ± 0.2	<0.8	0.7 ± 0.1	0.2 ± 0.1	0.2 ± 0.1
C III	1176[n]	150 ± 15	302 ± 30	80.8 ± 8.1	38.8 ± 4.5	36.6 ± 8.9	26.6 ± 2.7	13.4 ± 1.3

[a] Quiescent data only.
[b] ISM contamination.
[c] All three N III lines are blended in α Aql.
[d] N III 991.51 Å and 991.58 Å are blended.
[e] He II may be blended with neighboring N III lines.
[f] All three Fe III lines are blended in α Aql.
[g] C II is blended with O VI.
[h] Both S IV lines are blended.
[i] All N II lines are blended.
[j] N II 1084.57 Å is blended with N II 1084.85 Å.
[k] He II is blended with N II.
[l] All three N II lines are blended.
[m] The Fe III 1128.72 Å and 1129.19 Å are also blended.
[n] Combined flux for all six lines in multiplet: 1174.93, 1175.26, 1175.59, 1175.71, 1175.99, 1176.37 Å.

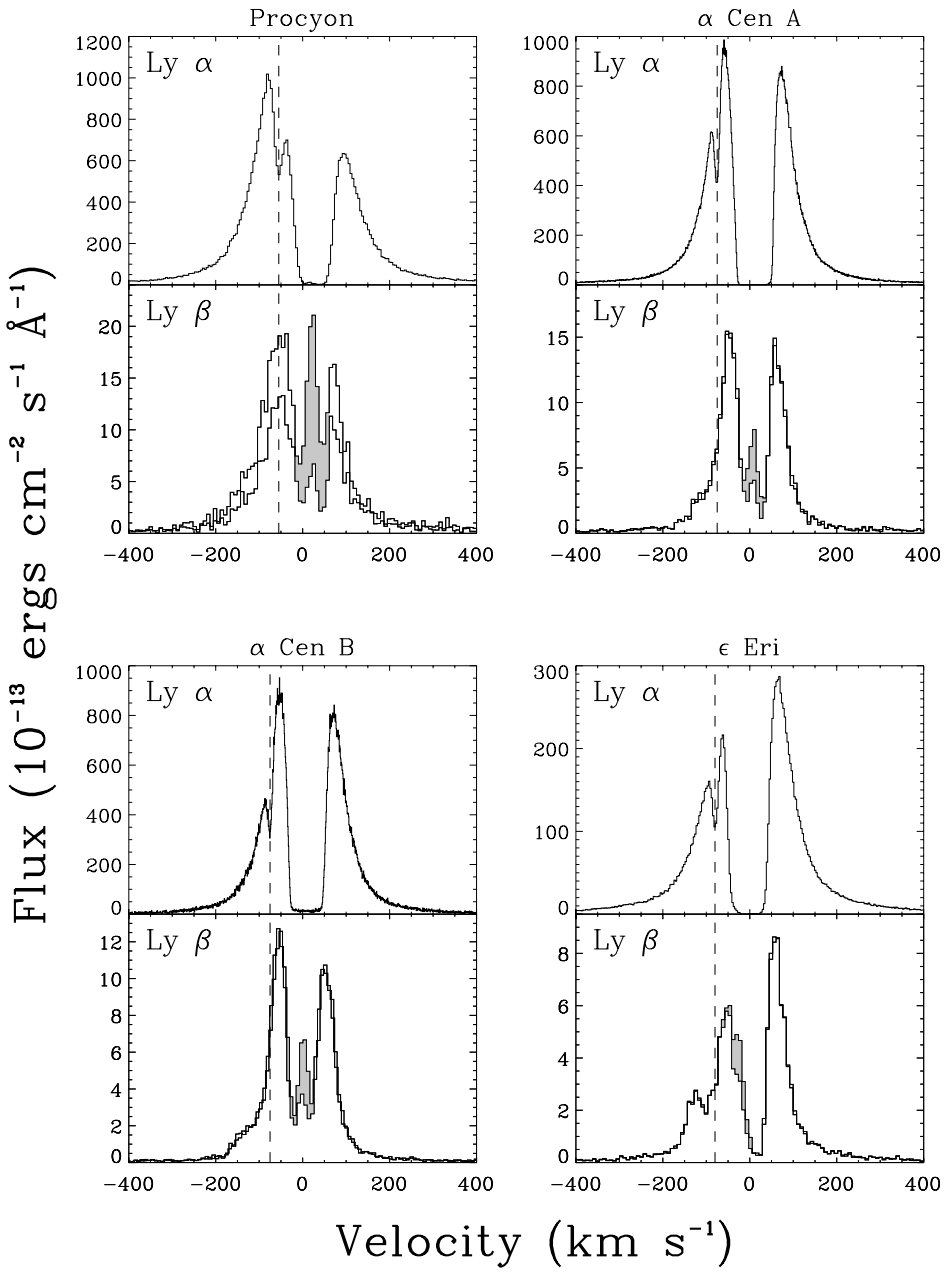

FIG. 4.—Comparison of Lyα (observed by *HST*) and Lyβ lines for four stars observed with the *FUSE* MDRS aperture. The full data set and nighttime-only data are shown. Shaded regions indicate the presence of H I and O I terrestrial airglow, although it is minimal for these observations. There is no indication of D I absorption (-82 km s^{-1} relative to H I) in Lyβ, whereas D I absorption is clearly present in the Lyα lines. Vertical dashed lines indicate the velocity of D I LISM absorption.

aperture. We did not use those *FUSE* exposures when the star was clearly out of the aperture, but it is difficult to establish whether a small flux decrease is due to true variability or a throughput decrease when the target is close to the edge of the MDRS. The instrumental explanation is supported by the *ORFEUS* observations, for which the star with the best agreement with *FUSE* for all lines is AB Dor, the only target in the combined data set observed through the LWRS. Aside from AB Dor, the majority (9/12) of measurements show higher fluxes from *ORFEUS* than *FUSE*, consistent with some loss of signal at times when the targets were close to the edge of the MDRS aperture. Nevertheless, intrinsic variability in stellar fluxes could also contribute to the differences.

4.1. *Electron Densities*

The ratio of the integrated flux of the C III 1176 Å multiplet to the C III 977 Å resonance line is sensitive to electron density, thereby providing estimates of transition region densities. In Table 6 we list the C III flux ratios and the electron densities computed using CHIANTI version 3.03 (Dere et al. 1997, 2001). Figure 7 displays the theoretical calculations and the flux ratio measurements. Because we do not have a detailed emission measure versus temperature distribution for these stars, we do not know the precise formation temperature for these lines. The mean electron density values listed in Table 6 are calculated using the most probable line formation temperature [$\log T(\mathrm{K}) \sim 4.92$], estimated

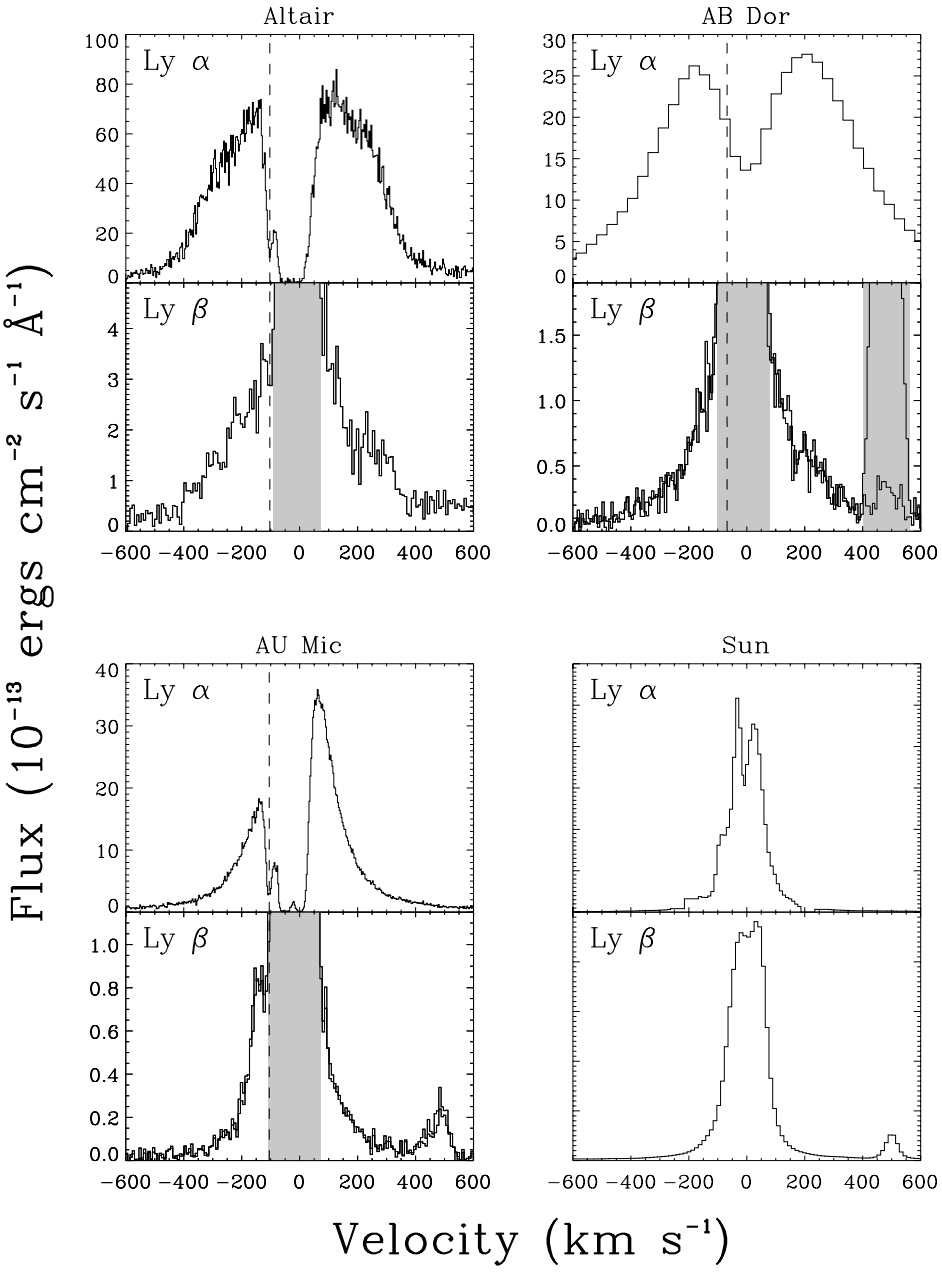

FIG. 5.—Same as Fig. 4, but for the three stars observed through the LWRS, and for comparison, the SUMER solar spectrum. Airglow dominates these *FUSE* spectra, although stellar emission is also present, as seen ~100 km s^{-1} from line center. AB Dor is the only target without a high-resolution Lyα observation.

from the centroids of the contribution functions (Brown et al. 1984; Jordan et al. 1987) and the ionization equilibrium calculations of Mazzotta et al. (1998). The 1 σ error bars listed in the first electron density column of Table 6 reflect errors assuming the most probable line formation temperature. The 1 σ error bars listed in the second electron density column bracket the range of likely C III formation temperatures, $4.74 \leq \log T(\mathrm{K}) \leq 5.05$. The C III 977 Å integrated flux of AB Dor has been corrected to replace the flux removed by LISM absorption, the only star to obviously show such absorption (see Fig. 8).

Although the error bars are large, the three most active stars, AB Dor, ϵ Eri, and AU Mic, have the highest C III flux ratios, whereas the four less active stars have low ratios. Transition region densities have been estimated using other lines for many of these stars. Wood, Linsky, & Ayres (1997) measured the electron density of α Cen A and B, using O IV] line flux ratios observed with the GHRS. They derived electron densities of $\log n_e = 9.65 \pm 0.20$ and $\log n_e = 9.50 \pm 0.30$ for α Cen A and B, respectively. The *FUSE* observations of α Cen A and B are consistent with these electron densities.

Three stars, AB Dor, ϵ Eri, and AU Mic, have large C III flux ratios with electron densities beyond the high-density limit. Jordan et al. (2001) estimated the electron density of ϵ Eri using numerous transition region lines in spectra obtained by STIS, and calculated an electron density of $\log n_e = 11.2 \pm 0.1$, which is within our 1 σ error bar. A C III flux ratio of 0.75–1.02 has been estimated for AB Dor with *ORFEUS II* data by Schmitt et al. (1998), and using *FUSE*

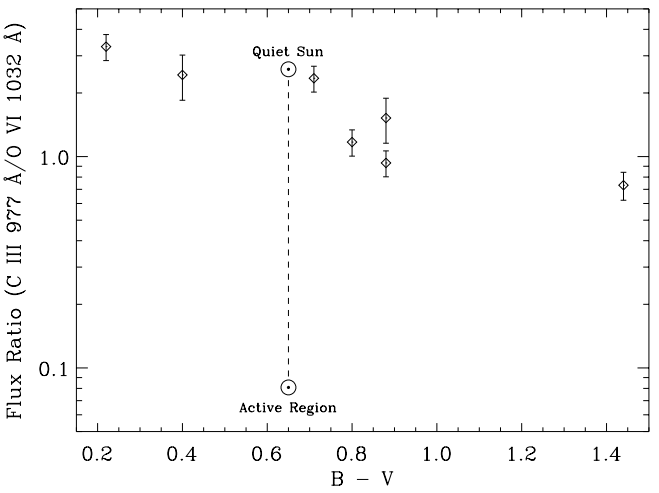

FIG. 6.—Flux ratio of C III 977 Å and O VI 1032 Å as a function of $B-V$. Solar values are presented for the quiet Sun and an active region.

data Ake et al. (2000) have reported a ratio of 0.65 ± 0.17, consistent with our measurements in Table 6. Brandt et al. (2001), on the other hand, determined an electron density for AB Dor using STIS spectra, obtaining $\log n_e \sim 12.4$. Maran et al. (1994) used the O V lines of AU Mic, observed by GHRS, as a density diagnostic and calculated an electron density of $\log n_e = 10.7$. The implied value of the electron density based on the C III flux ratio observed by *FUSE* is much larger than this estimate.

Because of opacity and temperature effects in active stars, the flux ratio of the C III lines ceases to provide a reliable diagnostic of the electron density (Del Zanna, Landini, & Mason 2002). For our most active stars, AB Dor, ϵ Eri, and AU Mic, the C III flux ratio probably does not correspond to a physically significant electron density. The *FUSE* observations confirm results from *HST* that α Cen A and B have $\log n_e \approx 9.6$ in their transition regions near $\log T(\mathrm{K}) = 4.8$. The *FUSE* observations also demonstrate the difficulty of using the C III flux ratio to estimate the electron density for the most active stars.

5. LINE PROFILES

Linsky & Wood (1994) recognized that high-resolution profiles of C IV 1548 and 1550 Å and Si IV 1394 and 1403 Å in GHRS spectra of AU Mic have broad wings extending to ± 200 km s^{-1} and therefore cannot be modeled with single Gaussian profiles. Instead, they found that fitting these lines with double Gaussians was successful for line profiles of AU Mic and other stars, such as α Cen A and B (Wood et al. 1997). Vilhu et al (1998) fitted double Gaussians to transition region lines in AB Dor, and found even broader profiles during flares. Ake et al. (2000) found that the *FUSE* profile of the O VI 1032 Å line of AB Dor also could not be modeled by a single Gaussian owing to the presence of very broad wings. Instead, they fitted double Gaussians with a narrow component full-width at half-maximum (FWHM) equal to about 80 km s^{-1} and a broad component of 300 km s^{-1}. They cautioned that these values were preliminary because the *FUSE* instrumental line spread function was not known accurately at that time. Nevertheless, the O VI widths are similar to what Vilhu et al (1998) found for the C IV lines of AB Dor in GHRS spectra. Young et al. (2001) note that the O VI lines of Capella are also very broad. Solar observations have long indicated that transition region profiles require

TABLE 4
ORFEUS SPECTRA

Star Name	Observation Date	Wavelength Range (Å)	C III Flux[a] (977 Å) (10^{-14} erg cm^{-2} s^{-1})	O VI Flux[a] (1032 Å) (10^{-14} erg cm^{-2} s^{-1})	C III Flux[a] (1176 Å) (10^{-14} erg cm^{-2} s^{-1})
Procyon	1993 Sep 16	860–1180	750.9 ± 16.3 (+40%)	277.4 ± 9.6 (+24%)	384.9 ± 16.4 (+24%)
	1996 Nov 29	910–1220	718.0 ± 6.2 (+32%)	267.3 ± 3.7 (+20%)	377.2 ± 5.8 (+21%)
α Cen A.....	1993 Sep 17	860–1187	244.0 ± 5.9 (+9%)	81.9 ± 3.9 (−14%)	...
AB Dor.....	1996 Nov 26	860–1187	51.3 ± 1.5 (+1%)	41.5 ± 0.9 (−8%)	35.3 ± 1.1 (−9%)
α Cen B.....	1993 Sep 17	860–1180	78.8 ± 11.9 (−16%)	93.8 ± 10.3 (+52%)	...
ϵ Eri	1993 Sep 16	860–1187	32.6 ± 4.6 (−19%)	48.4 ± 4.0 (+11%)	...

[a] Includes percent difference between the *ORFEUS* and *FUSE* fluxes for the emission line. A positive number indicates that the *ORFEUS* fluxes are larger than those measured by *FUSE*.

TABLE 5
HST SPECTRA THAT INCLUDE THE C III 1176 Å MULTIPLET

Star Name	Instrument	Observation Date	Grating	Resolution (km s^{-1})	Wavelength (Å)	C III Flux[a] (10^{-14} erg cm^{-2} s^{-1})
Altair	GHRS	1996 Aug 29	G140L	150	1152–1448	151.9 ± 5.2 (−3%)
α Cen A.....	STIS	1999 Dec 22	E140H	2.6	1140–1335	107.4 ± 0.8 (+21%)
AB Dor.....	GHRS	1994 Nov 16	G140L	150	1161–1448	44.4 ± 0.9 (+14%)
ϵ Eri	STIS	2000 Mar 18	E140M	6.6	1140–1735	34.5 ± 0.9 (+18%)
AU Mic.....	STIS	1998 Oct 23	E140M	6.6	1150–1735	14.5 ± 0.4 (+7%)

[a] Includes percent difference between the *HST* and *FUSE* fluxes for the C III 1176 Å multiplet. A positive number indicates that the *HST*/STIS or GHRS fluxes are larger than those measured by *FUSE*.

TABLE 6
ELECTRON DENSITIES FROM C III 1176 Å/C III 977 Å

Star	Flux Ratio[a]	$\log n_e$[b] (cm^{-3})	$\log n_e$[c] (cm^{-3})
Altair	0.551 ± 0.078	$10.2^{+0.6}_{-0.3}$	$10.2^{+5.4}_{-0.4}$
Procyon	0.556 ± 0.078	$10.3^{+0.7}_{-0.3}$	$10.3^{+5.5}_{-0.4}$
α Cen A.....	0.361 ± 0.051	$9.54^{+0.16}_{-0.17}$	$9.54^{+0.35}_{-0.18}$
AB Dor[d]	0.74 ± 0.11[e]	$15.5^{+0.6}_{-4.7}$	$15.5^{+\infty}_{-4.9}$
α Cen B.....	0.39 ± 0.11	$9.64^{+0.38}_{-0.39}$	$9.64^{+0.77}_{-0.39}$
ϵ Eri	0.658 ± 0.093[e]	$12.6^{+2.9}_{-2.3}$	$12.6^{+4.2}_{-2.4}$
AU Mic.....	0.88 ± 0.12[e]	16.1 ± 0.6	$16.1^{+\infty}_{-1.0}$

[a] Flux (in ergs cm^{-2} s^{-1}) ratio.
[b] Based on line formation temperature $\log T(\mathrm{K}) = 4.92$.
[c] Based on line formation temperature range $4.74 \leq \log T(\mathrm{K}) \leq 5.05$.
[d] C III 977 Å profile corrected for LISM absorption feature.
[e] Flux ratio beyond the high-density limit; therefore, estimated electron density likely has no physical significance due to opacity and temperature effects.

double Gaussian fits. A recent analysis of SUMER spectra by Peter (2001) demonstrates that two Gaussians are commonly needed to fit solar line profiles formed at temperatures from 40,000 to 10^6 K.

The best physical interpretation of the presence of broad and narrow Gaussian components in high-temperature emission lines remains elusive. Wood et al. (1997) suggested that the broad component likely is produced by high-velocity nonthermal motions during magnetic reconnection events, often called explosive events or microflares. This suggestion is supported by numerous similarities between stellar line profiles and the spectroscopic characteristics of solar explosive events (Dere, Bartoe, & Brueckner 1989). Wood et al. (1997) argued that these diagnostics could be used to study the heating mechanisms in stellar outer atmospheres, based on observations of Si IV and C IV from *HST*. It does not appear, however, that explosive events alone can account for all the broad emission that is seen in stellar and "mean" solar profiles. Therefore, other mechanisms have been invoked to explain the observed broad Gaussian component. For example, Peter (2000) discusses the possibility that the narrow components originate in small loops anchored in the solar network, while the broad components are formed in large coronal loops that span several network elements or in coronal funnels that open directly into the corona. Another mechanism used to explain the broad component in profiles observed in spectra of AB Dor is that the broad emission at high Doppler shifts can originate in extended material above the stellar surface that rotates significantly faster than the stellar photosphere (Vilhu et al. 1998; Ake et al. 2000). However, this mechanism is applicable only to rapidly rotating stars, and cannot explain the presence of the broad component in the slowly rotating stars in our sample. Strong emission lines in the *FUSE* spectral region allow detailed analysis of line profiles. In particular, the O VI profiles provide an opportunity to expand the analysis of double Gaussian fits to higher temperatures.

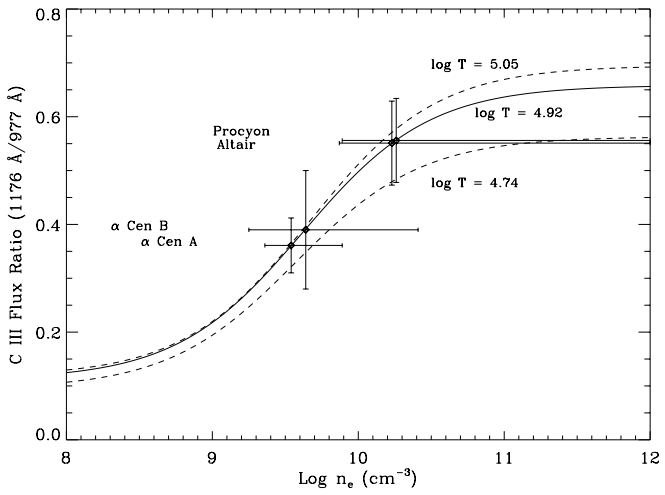

FIG. 7.—Flux (in ergs cm^{-2} s^{-1}) ratio of the C III 1176 Å multiplet and C III 977 Å. Theoretical curves of electron density as a function of C III flux ratio are CHIANTI calculations at the line formation temperature $\log T(\mathrm{K}) = 4.92$ (*solid line*). However, C III can be formed within a range of temperatures $4.74 \leq \log T(\mathrm{K}) \leq 5.05$ (*dashed lines*). Four stars are labeled at their observed flux ratio; the vertical error bars indicate the observed flux ratio error, and horizontal error bars reflect the measurement error and the range of possible formation temperatures. The three stars with high flux ratios (AB Dor, ϵ Eri, and AU Mic), are beyond the range of this plot. Their inferred electron densities are likely not physically significant, due to opacity and temperature effects.

We modeled the strongest lines in the *FUSE* spectrum (C III 977.02 Å, O VI 1031.93 and 1037.62 Å, and the components of the C III multiplet centered at 1176 Å) with single and double Gaussians, by χ^2 minimization (Bevington & Robinson 1992). The resulting fits are depicted in Figures 8–10. The need for a double Gaussian fit often is obvious from simple visual inspection, as is the case for the O VI lines of AB Dor. For all line profiles, we used the *F*-test (Bevington & Robinson 1992) in order to determine whether or not the reduction of χ^2 from a single to a double Gaussian fit is statistically significant. The resulting fit parameters (central velocity, v [km s^{-1}]; integrated flux, f [ergs cm^{-2} s^{-1}]; FWHM [km s^{-1}]) are listed in Tables 7, 8, and 9. The 1 σ measurement errors in the tables were estimated using Monte Carlo techniques. We subtracted a fit to the continuum level, when necessary, prior to the fitting the line profiles, using line-free regions adjacent to the emission line. The instrumental broadening was incorporated by convolving each synthetic profile with the instrumental line-spread function (Wood et al. 2002a). Altair and AB Dor have large rotational velocities with respect to the spectral resolution of *FUSE*. We convolved the synthetic profiles for these stars with a rotational broadening function appropriate for their $v \sin i$ (see Table 1). Both instrumental and rotational broadening are incorporated into the fitting routine, so that the final fit to the data includes the convolution of these profiles, and the fit parameter (b [km s^{-1}]) describes the intrinsic stellar Doppler line width, prior to convolution with rotational or instrumental broadening. Section 7 discusses the unique shape of Altair's line profiles.

In Table 10, parameters of the narrow and broad Gaussian components of C III 977 Å, C III 1176 Å, and O VI 1032, 1038 Å are presented for six of the dwarf stars. For the C III and O VI multiplets, the entries in Table 10 represent flux-weighted averages. Only C III 977 Å and the O VI doublet were strong enough to be modeled by double Gaussians. The C III 1176 Å multiplet components are too blended to yield any information concerning the broad components. Based on the C IV and Si IV lines, Wood et al. (1997) found that the ratio of the broad component flux to the total flux increased with stellar activity. Figure 11 depicts the ratio of

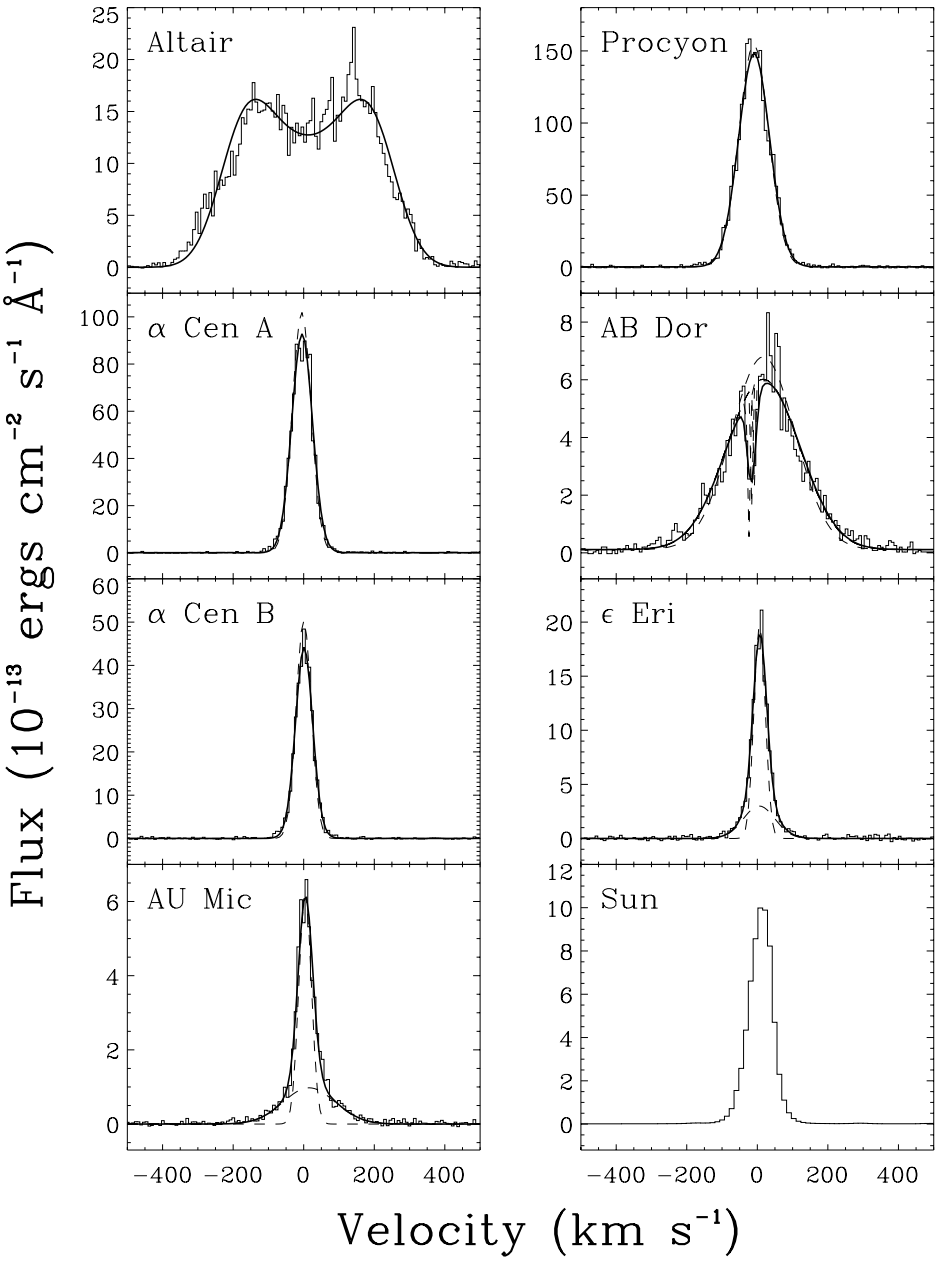

FIG. 8.—C III 977.020 Å line profiles for the seven stars observed by *FUSE* and the average quiet Sun, plotted on a heliocentric velocity scale. Dashed lines show single or double Gaussian fits. Solid lines show the sum of these fits convolved with the instrumental line spread function. Note the rotationally broadened and limb-brightened profile fit (*solid line*) for Altair.

the broad component flux to the total flux for O VI, as a function of C IV surface flux (see Table 10) and X-ray surface flux (see Table 1), both of which are spectral proxies for the heating rate and thus stellar activity in the transition region and corona, respectively. The correlation between the heating rate and the relative importance of the broad component holds for O VI when compared with the transition region heating rate as measured by the C IV surface flux. Procyon has a much larger broad component than would be expected from its X-ray activity level, but Procyon is an "X-ray–deficient" star that is underluminous in coronal emissions compared with transition region lines (Simon & Drake 1989). It also shows a broad component in only the hottest transition region emission line observed by *HST*, N V, but not in C IV or Si IV (Wood et al. 1996). A broad component in C III 977 Å was only required in two of the six stars, ϵ Eri and AU Mic. The more active star, AU Mic, does have a more prominent broad component than ϵ Eri.

As discussed in the Appendix, the relative velocity scale within each segment is very good, despite the difficulty in determining the absolute scale. Except for Procyon and AU Mic, there is relatively little velocity shift between the narrow and broad components, as seen in Table 10. Regardless of the precise nature of the formation mechanism of the broad component, observations have indicated that the broad component is more likely to be blueshifted relative to the narrow component, rather than redshifted (Dere et al. 1989; Peter 2000, 2001). The broad component in the O VI

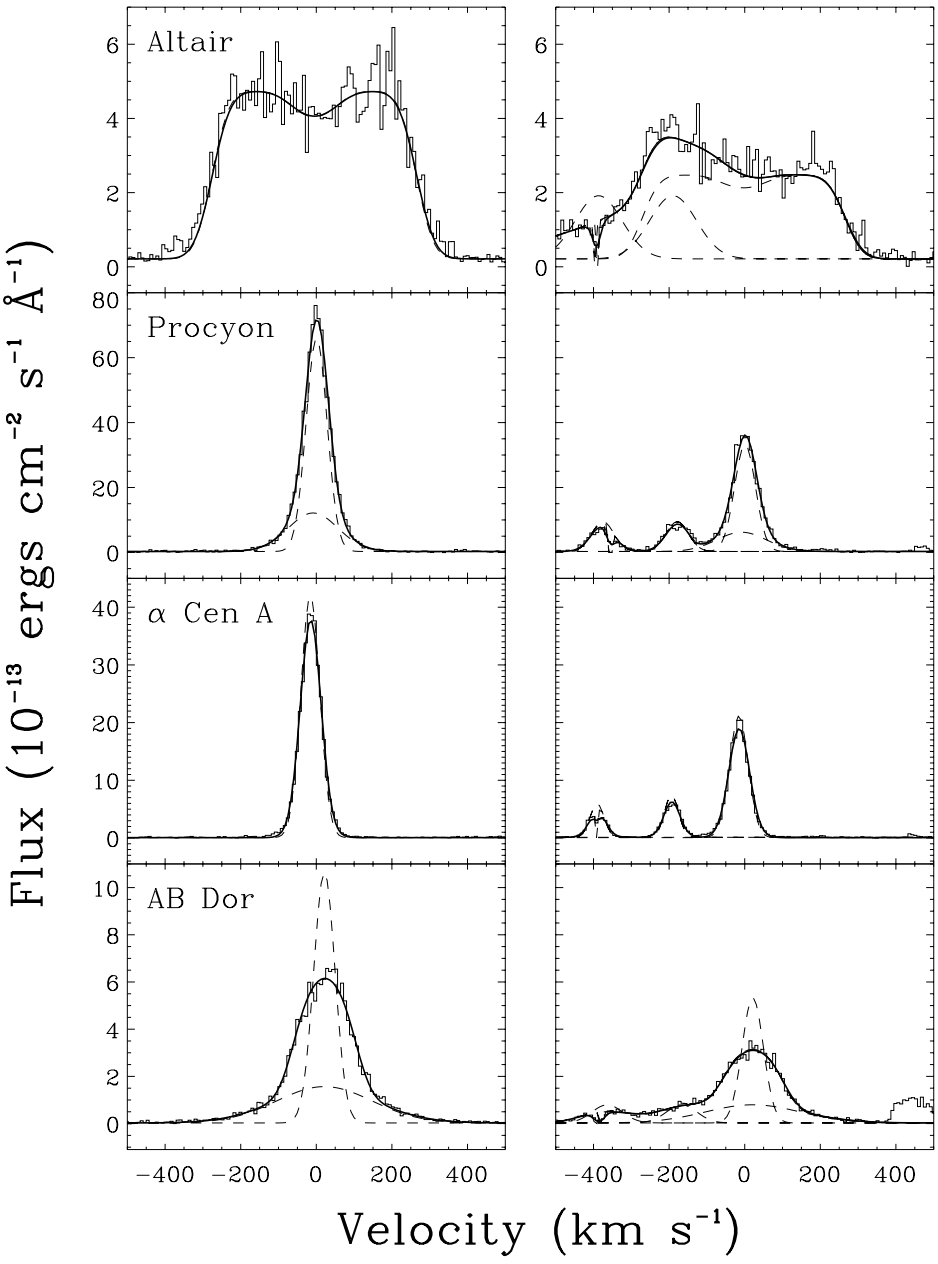

FIG. 9*a*

FIG. 9.—(*a*) O VI 1031.925 Å (*left column*) and O VI 1037.614 Å (*right column*) line profiles for four of the seven stars on a heliocentric velocity scale. Dashed lines show the Gaussian fits to the O VI lines, and adjacent C II 1036.3367 Å and 1037.0182 Å lines. Solid lines are the sums of the fits convolved with the instrumental line spread function. For Altair, a rotationally broadened limb-brightened profile was used. (*b*) Same as (*a*), but for the remaining three stars and the average quiet Sun.

Procyon spectrum is clearly blueshifted relative to the narrow component, whereas the broad component in the AU Mic spectrum is highly redshifted. This large redshift of the C III and O VI broad component relative to the narrow component in AU Mic is consistent with component velocity differences for other transition region lines observed by *HST*/STIS (Pagano et al. 2000). We discuss the Doppler shifts found in the *FUSE* spectrum in the next section.

Table 10 lists nonthermal velocities of the narrow components of C III 977 Å, the C III 1176 Å multiplet, and O VI 1032 Å, and likewise of the broad components, when present. We convert the widths of the narrow and broad components to nonthermal velocities using the relation (in cgs units)

$$\left(\frac{\Delta\lambda}{\lambda}\right)^2 = 3.08 \times 10^{-21}\left(\frac{2kT}{m_i} + \xi^2\right), \qquad (1)$$

where $\Delta\lambda$ is the measured FWHM, T is the line formation temperature, m_i is the ion mass, and ξ is the most probable nonthermal speed. Although no broad components were modeled for the C III 1176 Å multiplet, because of the heavy blending, the widths of the single Gaussian fits help interpret the C III 977 Å line profile. Wood et al. (1996) point out the additional broadening of stellar emission lines in the Procyon spectrum that can occur when the lines become

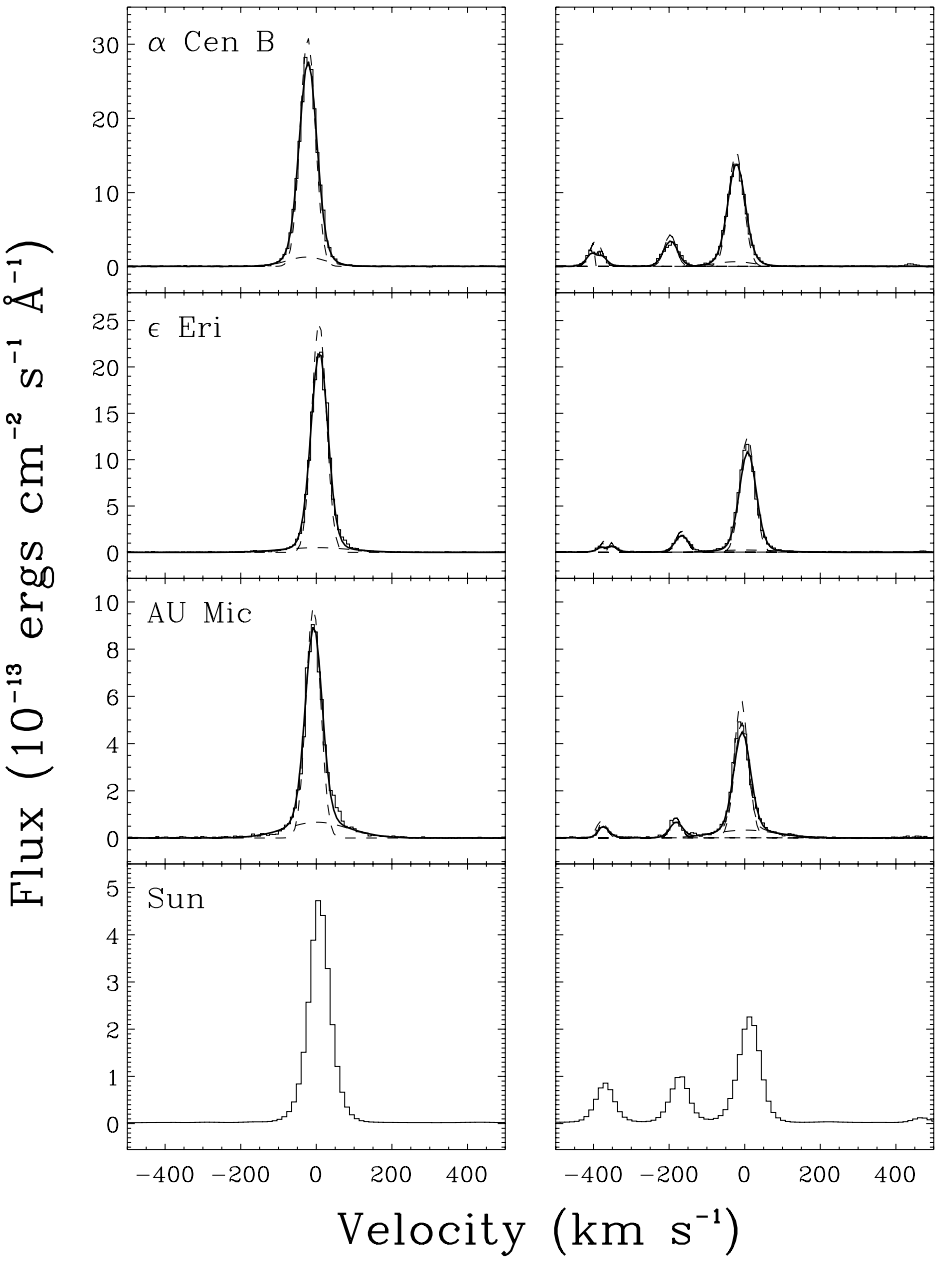

FIG. 9*b*

optically thick. This opacity broadening could lead to an overestimate of the nonthermal broadening when it is not carefully accounted for. Comparing widths of optically thin lines of similar excitation is a simple test of the importance of opacity broadening. In the O VI doublet, for example, the two lines have a factor of 2 different opacities, but the same widths (see Table 8). Likewise, we can compare the width of C III 977 Å with those of the (optically thin) lines in the C III 1176 Å multiplet. For the three hottest stars in Table 10, it is clear that the inferred nonthermal velocity of C III 977 Å is significantly larger than C III 1176 Å. By comparison, the three coolest stars have consistent C III nonthermal velocities, and are thus probably not affected by opacity broadening.

The strong transition region emission profiles available in the *FUSE* spectral region (C III 977 Å and O VI) are critically important for the analysis of line profile parameters over a wide range of temperatures, when combined with the high-S/N line profiles available in the *HST* spectral region (e.g., Si IV, C IV, and N V). Figure 12 compares the ratio of the broad component to the total line flux as a function of line formation temperature. The solar data are taken from Peter (2001). As shown earlier in Figure 11, the most active stars are more likely to require a double Gaussian to fit the line profile. In Figure 12 we show an active star (AU Mic) that requires double Gaussian fits over the entire line formation temperature range from Si IV [$\log T(\mathrm{K}) \sim 4.75$] to O VI [$\log T(\mathrm{K}) \sim 5.45$]. There appears to be a decrease in the strength of the broad component as the formation temperature increases, which is the opposite behavior from Procyon, which (as mentioned previously) requires double Gaussian fits only for the lines formed hotter than $\log T(\mathrm{K}) \sim 5.25$ (N V and O VI). In Procyon, the ratio of the broad component to the total flux is almost identical for N V and O VI. In

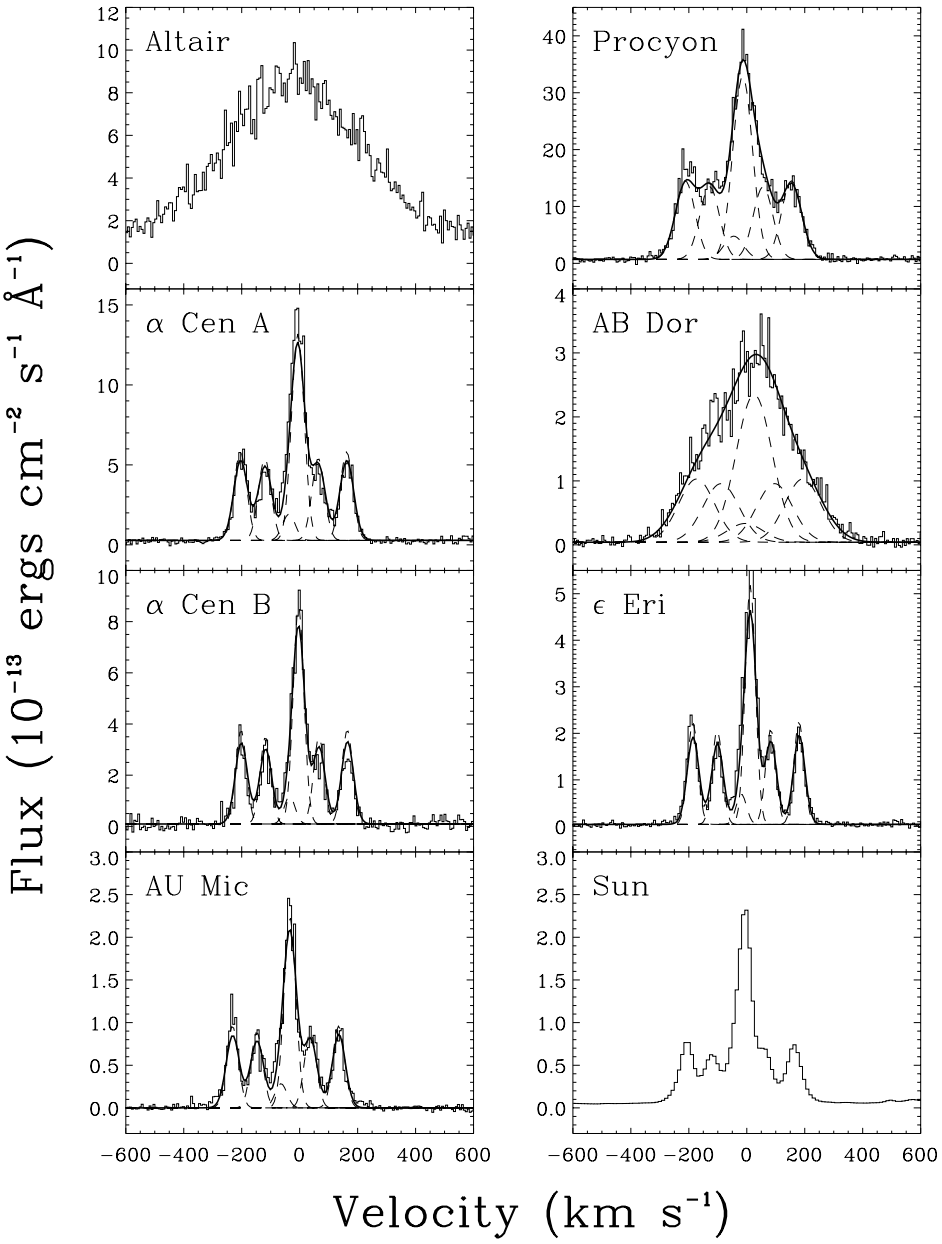

FIG. 10.—C III 1176 Å multiplet on a heliocentric velocity scale, where zero velocity is for the 1175.70 Å component. Dashed lines depict the single Gaussian fits, and the solid line is a sum of the fits convolved with the instrumental line-spread function.

the solar case, the relative importance of the broad component peaks at the formation temperature of C IV (~28%), whereas the broad component can contain more than 50% (Si IV) of the line flux in AU Mic. Figure 12 displays the nonthermal velocities for the broad and narrow components. Although the variation of nonthermal velocity with formation temperature is slightly different for AU Mic and the Sun, the variation between the broad and narrow components of each object individually is very similar. The velocity separation of the broad and narrow component centroids for the Sun and AU Mic are shown in the bottom panel of Figure 12. The broad component is consistently redshifted relative to the narrow component for AU Mic (resulting in a negative value for v[narrow] – v[broad]), while the Sun shows the opposite behavior: the broad component is blueshifted relative to the narrow component (resulting in a positive value for v[narrow] – v[broad]). Despite this, relative shifts between the two components seem to have similar behavior as a function of line formation temperature.

Figure 13 illustrates transition region nonthermal velocities, as measured from the O VI 1032 Å and C III 977 Å lines, versus stellar surface gravity. The broad components are displayed with triangles, and the narrow components with diamonds. Dashed lines indicate the sound speed at the line formation temperature. *In almost all cases, the broad components are supersonic, and show no obvious trend with stellar gravity. The narrow components, however, are subsonic and do exhibit a trend toward larger nonthermal velocities with decreasing surface gravity.* As discussed above, opacity broadening may affect the C III 977 Å line, but there is no

TABLE 7
GAUSSIAN FIT PARAMETERS FOR C III 977.02 Å

Star	v[a] (km s^{-1})	Flux[b] (10^{-14} erg cm^{-2} s^{-1})	FWHM (km s^{-1})
Single Gaussian Fits			
Procyon	2 ± 10	535 ± 54	99.2 ± 5.0
α Cen A.....	9 ± 10	221 ± 22	62.9 ± 5.0
AB Dor[c]....	16.2 ± 5.0	50.3 ± 5.0	208 ± 11
α Cen B.....	5 ± 10	89.0 ± 8.9	50.5 ± 5.0
Double Gaussian Fits			
ϵ Eri	3 ± 10	26.7 ± 2.7	37.7 ± 5.0
	1 ± 10	10.8 ± 1.7	113.1 ± 8.3
AU Mic[d] ...	-1 ± 10	8.99 ± 0.90	41.7 ± 5.0
	13 ± 10	6.16 ± 0.64	172 ± 21

[a] Relative to the radial velocity of the stellar photosphere.
[b] Integrated flux based on Gaussian fits.
[c] LISM absorption present, flux corrected for LISM feature.
[d] Quiescent data only.

evidence for it in the O VI lines. We also have included the nonthermal velocities derived from optically thin lines in the C III 1176 Å multiplet (see Fig. 10 and Table 9). For the three stars with subsolar surface gravity (Procyon, α Cen A, and AB Dor), the C III 977 Å line appears to be influenced by opacity broadening, and our values for the nonthermal

TABLE 8
GAUSSIAN FIT PARAMETERS FOR O VI

Star	λ_{rest} (Å)	v[a] (km s^{-1})	Flux[b] (10^{-14} erg cm^{-2} s^{-1})	FWHM (km s^{-1})
Single Gaussian Fits				
α Cen A....	1031.9261	12.0 ± 5.0	90.8 ± 9.1	57.6 ± 5.0
	1037.6167	11.6 ± 5.0	44.8 ± 4.5	56.5 ± 5.0
Double Gaussian Fits				
Procyon ...	1031.9261	9.6 ± 5.0	142 ± 14	61.6 ± 7.6
	1031.9261	4.1 ± 5.0	83 ± 30	145 ± 21
	1037.6167	9.1 ± 5.0	74 ± 15	62.5 ± 6.5
	1037.6167	1 ± 19	40 ± 14	163 ± 46
AB Dor	1031.9261	19.9 ± 5.0	26.1 ± 2.6	66 ± 13
	1031.9261	22.6 ± 5.4	17.0 ± 2.1	310 ± 21
	1037.6167	19.0 ± 5.0	12.9 ± 1.5	63 ± 12
	1037.6167	22 ± 13	8.6 ± 1.3	300 ± 35
α Cen B....	1031.9261	0.1 ± 5.0	50.6 ± 5.1	45.7 ± 5.0
	1031.9261	-0.9 ± 5.0	8.4 ± 3.3	104 ± 14
	1037.6167	-0.1 ± 5.0	24.2 ± 2.6	44.8 ± 5.0
	1037.6167	-3 ± 14	5.0 ± 2.4	101 ± 18
ϵ Eri	1031.9261	9.7 ± 5.0	40.3 ± 4.0	44.4 ± 5.0
	1031.9261	14.1 ± 7.8	4.92 ± 0.88	172 ± 26
	1037.6167	8.3 ± 5.0	20.3 ± 2.0	43.5 ± 5.0
	1037.6167	10 ± 28	2.77 ± 0.84	176 ± 49
AU Mic[c] ..	1031.9261	0.1 ± 5.0	14.7 ± 1.9	42.3 ± 5.1
	1031.9261	15 ± 25	6.1 ± 2.4	158 ± 33
	1037.6167	-1.1 ± 5.0	7.78 ± 0.82	41.5 ± 5.0
	1037.6167	12.8 ± 8.4	2.9 ± 1.0	153 ± 33

[a] Relative to the radial velocity of the stellar photosphere.
[b] Integrated flux based on Gaussian fits.
[c] Quiescent data only.

TABLE 9
GAUSSIAN FIT PARAMETERS FOR C III (1176 Å)

Star	λ_{rest} (Å)	v[a] (km s^{-1})	Flux[b] (10^{-14} erg cm^{-2} s^{-1})	FWHM (km s^{-1})
Single Gaussian Fits				
Procyon ...	1174.933	...	45.6 ± 7.0	75.9 ± 7.4
	1175.263	...	47 ± 14	91 ± 33
	1175.590	...	18.4 ± 7.7	88 ± 34
	1175.711	...	102 ± 10	77.2 ± 5.2
	1175.987	...	42.2 ± 4.6	81 ± 12
	1176.370	...	45.4 ± 4.5	79.3 ± 5.2
α Cen A....	1174.933	6.6 ± 5.0	12.4 ± 1.2	51.3 ± 5.0
	1175.263	7.5 ± 5.0	9.8 ± 1.2	47.6 ± 8.3
	1175.590	10 ± 16	7.8 ± 3.6	61 ± 23
	1175.711	4.9 ± 5.0	28.9 ± 4.1	52.1 ± 5.3
	1175.987	5.1 ± 6.5	9.6 ± 2.2	51 ± 12
	1176.370	5.6 ± 5.0	11.4 ± 1.1	49.8 ± 5.0
AB Dor	1174.933	...	6.8 ± 1.3	151 ± 28
	1175.263	...	6.1 ± 1.6	145 ± 49
	1175.590	...	2.8 ± 1.9	175 ± 54
	1175.711	...	12.2 ± 3.6	119 ± 46
	1175.987	...	5.5 ± 1.5	134 ± 36
	1176.370	...	6.4 ± 1.3	151 ± 28
α Cen B....	1174.933	...	5.86 ± 0.44	40.5 ± 5.0
	1175.263	...	5.17 ± 0.75	40.2 ± 5.8
	1175.590	...	4.3 ± 3.5	82 ± 57
	1175.711	...	15.2 ± 2.8	43.0 ± 8.2
	1175.987	...	5.23 ± 0.73	42.7 ± 5.9
	1176.370	...	5.72 ± 0.46	43.0 ± 5.0
ϵ Eri	1174.933	-0.9 ± 5.0	4.16 ± 0.42	41.7 ± 5.0
	1175.263	1.2 ± 5.0	2.96 ± 0.47	35.9 ± 5.8
	1175.590	2 ± 13	2.9 ± 2.6	56 ± 24
	1175.711	2.4 ± 5.0	9.1 ± 2.5	39 ± 10
	1175.987	1.6 ± 5.0	3.41 ± 0.45	40.8 ± 6.9
	1176.370	2.4 ± 5.0	3.55 ± 0.29	39.4 ± 5.0
AU Mic[c] ..	1174.933	-5 ± 15	2.09 ± 0.39	45 ± 11
	1175.263	-4 ± 18	1.68 ± 0.29	43 ± 11
	1175.590	-8 ± 47	1.33 ± 0.88	59 ± 33
	1175.711	-4.6 ± 6.2	4.04 ± 0.76	40 ± 11
	1175.987	-3 ± 15	1.93 ± 0.36	49 ± 11
	1176.370	-5 ± 15	1.86 ± 0.31	46 ± 11

[a] Relative to the radial velocity of the stellar photosphere.
[b] Integrated flux based on Gaussian fits.
[c] Quiescent data only.

velocity are likely to be overestimates. Wood et al. (1997) demonstrated that the nonthermal velocity of the narrow component depends on stellar surface gravity as a power law. Their fit to the Si IV and C IV data is the dotted line in Figure 13. The best fit to the O VI data is shown by the solid line:

$$\xi_{NC} = (23.7 \pm 1.7)\left(\frac{g}{g_\odot}\right)^{-0.43 \pm 0.12}, \qquad (2)$$

which differs only slightly from the Wood et al. (1997) result. Adding more stars and more transition region lines to the sample would help determine whether the dependence on gravity is independent of line formation temperature or ion.

6. DOPPLER SHIFTS

A curious property of transition region lines, emitted by ions abundant at temperatures between 2×10^4 and $\sim 8 \times 10^5$ K, is that they tend to be systematically redshifted

TABLE 10
LINE PROFILE PROPERTIES

STAR	$\log F_{C\,IV}$[a] (ergs cm^{-2} s^{-1})	f_{BC}/f_{tot}[b]		$v_{NC} - v_{BC}$ (km s^{-1})		ξ_{NC} (km s^{-1})			ξ_{BC} (km s^{-1})	
		C III	O VI	C III	O VI	C III (977)	C III (1176)	O VI	C III	O VI
Procyon ..	4.65	...	0.37 ± 0.09	...	6 ± 7	58.8 ± 3.0	47.7 ± 8.0	32.9 ± 5.0	...	89 ± 18
α Cen A...	3.73	...	...	...	...	36.6 ± 3.1	29.6 ± 5.2	29.2 ± 3.5	...	...
AB Dor ...	5.49	...	0.39 ± 0.04	...	-3 ± 7	124.6 ± 6.6	83.5 ± 24.2	35.0 ± 8.8	...	183 ± 16
α Cen B...	3.81	...	0.14 ± 0.05	...	1 ± 7	28.8 ± 3.2	26.1 ± 7.6	21.1 ± 4.1	...	59.3 ± 9.8
ϵ Eri	4.47	0.29 ± 0.04	0.11 ± 0.02	2 ± 7	-4 ± 7	20.6 ± 3.4	22.9 ± 6.1	20.1 ± 4.2	67.3 ± 5.0	103 ± 21
AU Mic...	5.28	0.41 ± 0.03	0.29 ± 0.09	-14 ± 7	-15 ± 7	23.2 ± 3.3	25.5 ± 8.8	18.4 ± 4.5	103 ± 13	92 ± 20

[a] All C IV surface fluxes, except for ϵ Eri, are based on measurements of both lines in the multiplet by Wood et al. 1997. We measured ϵ Eri directly from data in the *HST* public archive.
[b] Flux ratio of the broad component to the total flux (broad and narrow components).

compared to the photosphere and lower chromosphere. This property was seen in *Skylab* observations of the Sun (Doschek, Feldman, & Bohlin 1976), and subsequently was confirmed by other solar instruments and most recently by *SOHO*/SUMER. The solar data show an increase in redshift from essentially zero at $T \leq 10^4$ K to about 10 km s^{-1} at C IV temperatures (10^5 K). Extension of the redshift trend to higher temperatures has been controversial, owing to the uncertain rest wavelengths of UV lines of more highly ionized species. Brekke (2000) has summarized recent analyses of *SOHO*/SUMER observations of such lines as Ne VIII 770 Å ($T = 8 \times 10^5$ K) and Mg X 624 Å ($T = 1 \times 10^6$ K),

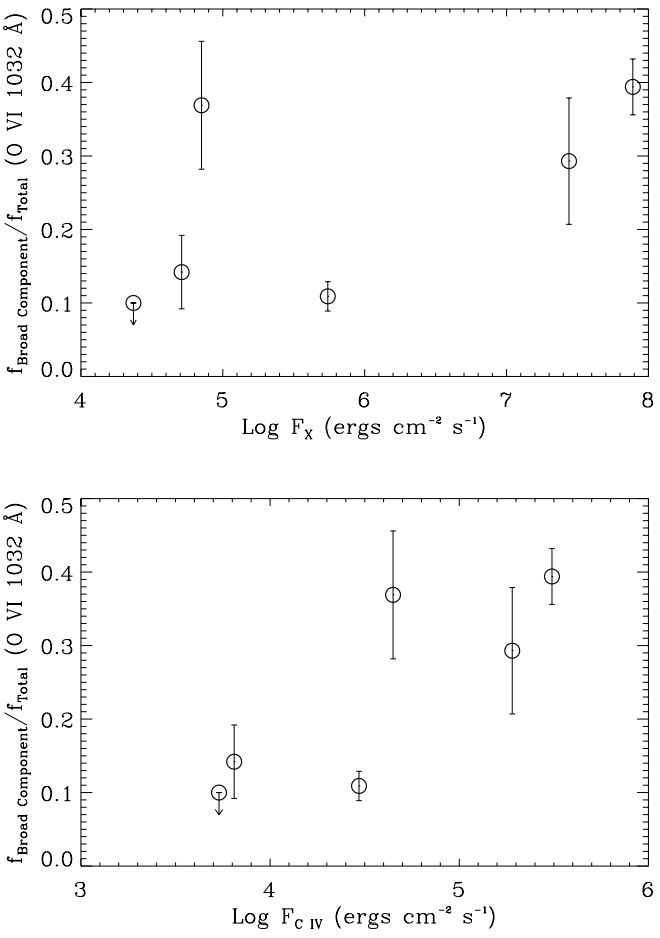

FIG. 11.—Ratio of the broad component to the total line flux for O VI 1032 Å, as a function of the X-ray surface flux (*top*; Table 1) and C IV surface flux (*bottom*; Table 10). There is a general positive correlation between the strength of the broad component and stellar activity as measured by these surface fluxes, which measure the mechanical heating rates.

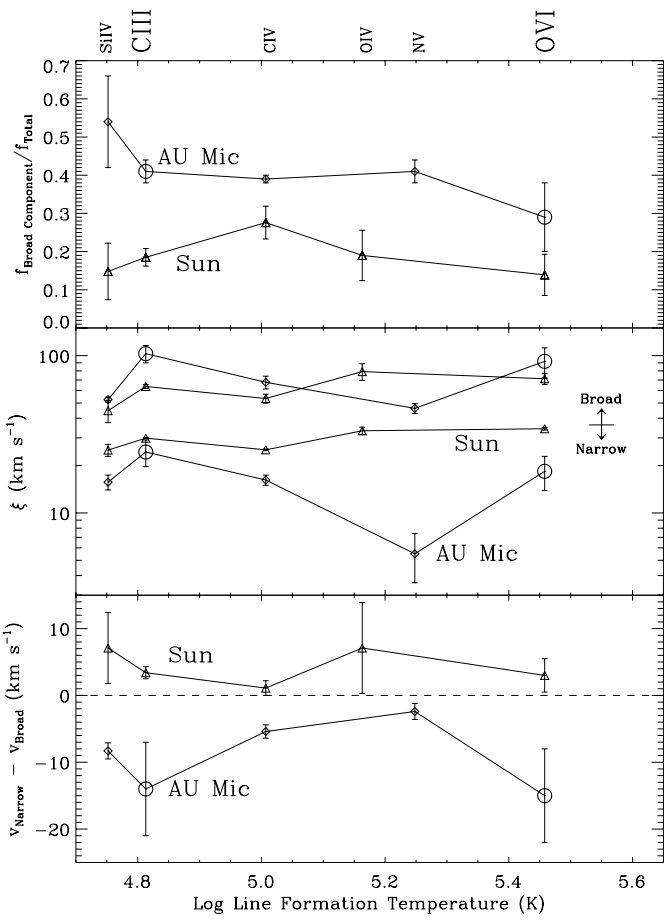

FIG. 12.—Comparison of three line profile diagnostics as a function of line formation temperature, for an active star in our sample, AU Mic, and the Sun. Top panel displays the ratio of broad component to total line flux for six transition region lines, with different formation temperatures. The *FUSE* lines are indicated by large open circles, and the *HST* lines by diamonds. The solar data presented by Peter (2001) are indicated by triangles. The AU Mic line fits were presented by Pagano et al. (2000). The species associated with each symbol are labeled at the top. The middle panel shows the nonthermal velocities for the broad (higher velocities) and narrow (lower velocities) components. The velocity separation of the narrow and broad components is displayed in the bottom panel.

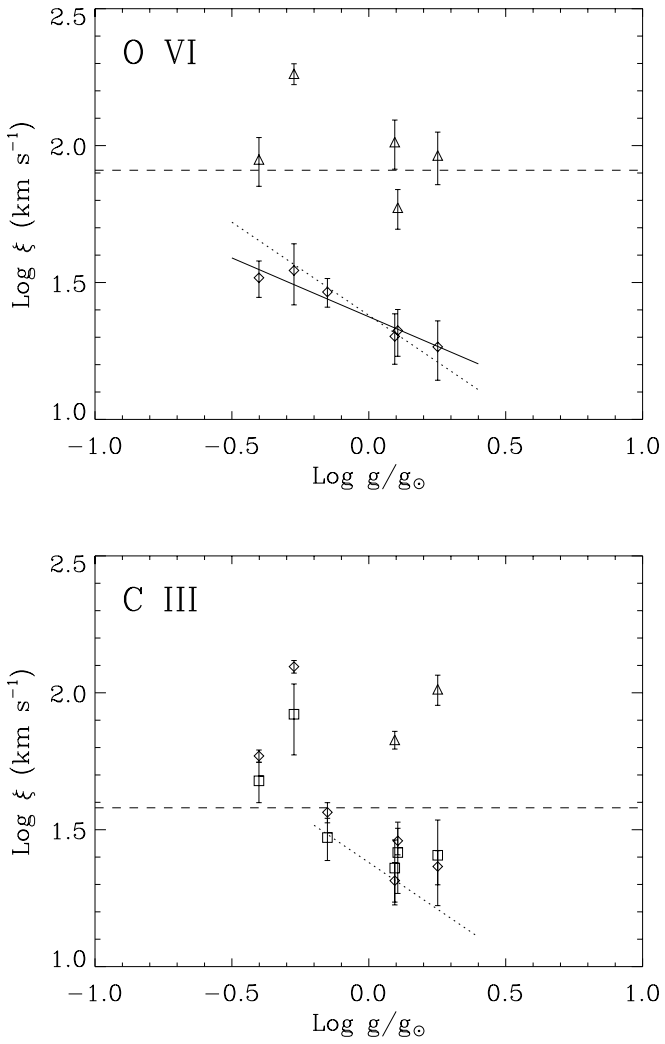

FIG. 13.—Nonthermal components of the line widths, plotted as a function of stellar surface gravity. Triangles represent broad components, and diamonds represent narrow components. Because C III 977 Å shows some evidence for opacity broadening, we include narrow components from the C III 1176 Å multiplet (*squares*). Dashed lines indicate the sound speed at the formation temperature. The solid line is our fit to the correlation of O VI narrow-component nonthermal velocity with stellar surface gravity. Dotted lines are the fit to the C IV and Si IV narrow-component nonthermal velocities presented by Wood et al. (1997).

which indicate that the peak redshift in the quiet Sun is at about 10 km s^{-1} near $T = 1 \times 10^5$ K and decreases with increasing temperature to become a blueshift for $T > 5 \times 10^5$ K (Peter & Judge 1999). If, as is generally assumed, the high-temperature lines are optically thin and the measured Doppler centroid reflects the emission-measure–weighted net flow speed in a highly dynamic atmosphere, then the empirical dependence of redshift with temperature provides an important constraint on stellar transition region dynamics.

The discovery of redshifted transition region lines in stellar spectra goes back to early observations with the *International Ultraviolet Explorer* (*IUE*) (Ayres & Linsky 1980; Ayres et al. 1983). Wood et al. (1997) summarized the very sensitive measurements of stellar redshifts made possible with GHRS. The stellar measurements provide a different perspective, since they are a full disk average, which is very difficult to achieve for solar measurements at high spectral resolution. Furthermore, the Pt wavelength calibration onboard lamps provide *IUE*, GHRS, and STIS with a precise wavelength scale, and the GHRS and STIS echelles have resolutions as high as 3.5 km s^{-1}. The best of the recent solar UV spectrographs (SUMER), however, lacks an internal wavelength standard, and the first-order resolution is only $\sim$25 km s^{-1}. The *HST* observations of α Cen A, α Cen B, and Procyon show a pattern similar to the Sun, with redshifts increasing from zero in the low chromosphere to about 10 km s^{-1} for the C IV lines. Between 10^5 and 2×10^5 K there is no clear trend, as the N V and O V] lines show an increase in redshift for Procyon, but a decrease for α Cen A and B. Complicating the analysis is the uncertain rest wavelengths of these lines, although the divergent trends of Procyon versus α Cen A and B do not depend on the precise rest wavelengths.

The *FUSE* spectral range contains the important Li-like O VI lines, formed at $T = 3 \times 10^5$ K, to extend the range hotter than C IV. However, accurate Doppler shift measurements are difficult with *FUSE* because there is no wavelength-calibration lamp on board the satellite. The absolute wavelength scale provided by the data reduction pipeline is uncertain by about $\pm$20 km s^{-1} (Sahnow et al. 2000), and the spectral resolution (about 15 km s^{-1}) is lower than the STIS medium-resolution echelle mode, thereby affecting the accuracy of the Doppler centroiding. In the Appendix we describe how the absolute wavelength scale can be improved to better than $\pm$5 km s^{-1} using LISM absorption lines. Ake et al. (2000) did not cite any radial velocity measurements for the AB Dor spectrum because of the uncertain velocity scale in the earlier version of the pipeline available at the time.

Figure 14 illustrates the Doppler offset relative to the stellar (photospheric) radial velocity for various ions as a function of formation temperature. Doppler shifts are based on Gaussian fits to strong stellar emission lines. *FUSE* measurements are depicted by large open circles, while those from *HST* are diamonds. Multiple lines from a single ion are represented by a flux-weighted mean. *HST* values for Procyon are taken from Wood et al. (1996), for α Cen A and α Cen B from Wood et al. (1997), for ϵ Eri from Jordan et al. (2001), and for AU Mic from Pagano et al. (2000). The solar data were obtained by SUMER (Peter & Judge 1999). When narrow and broad components were measured, their velocity shifts are represented by "n" and "b" symbols, respectively. Only AU Mic displays little deviation from the stellar photospheric rest velocity, indicated by the dashed lines at 0 km s^{-1}. Most stars show an increase in velocity offset with increasing line formation temperature. The Procyon velocities increase even up to O VI temperatures, whereas the α Cen B velocities increase to C III and O IV temperatures, but then decrease with increasing temperature beyond that point. As discussed above, the solar line shifts have the same general behavior (Peter & Judge 1999). However, the O VI line shift in α Cen A and ϵ Eri is highly redshifted with respect to other high-temperature lines, such as O V. Because we pegged the absolute wavelength scale to C II 1036.3367 Å, directly adjacent to the O VI lines, we believe that the wavelength calibration in this spectral region is very well determined, and the redshift in the O VI line is reliable. The velocity shift between the broad and narrow components is given in Table 10. Typically, the narrow components are redshifted relative to the broad component until the trend is reversed in the coolest stars. For example, in

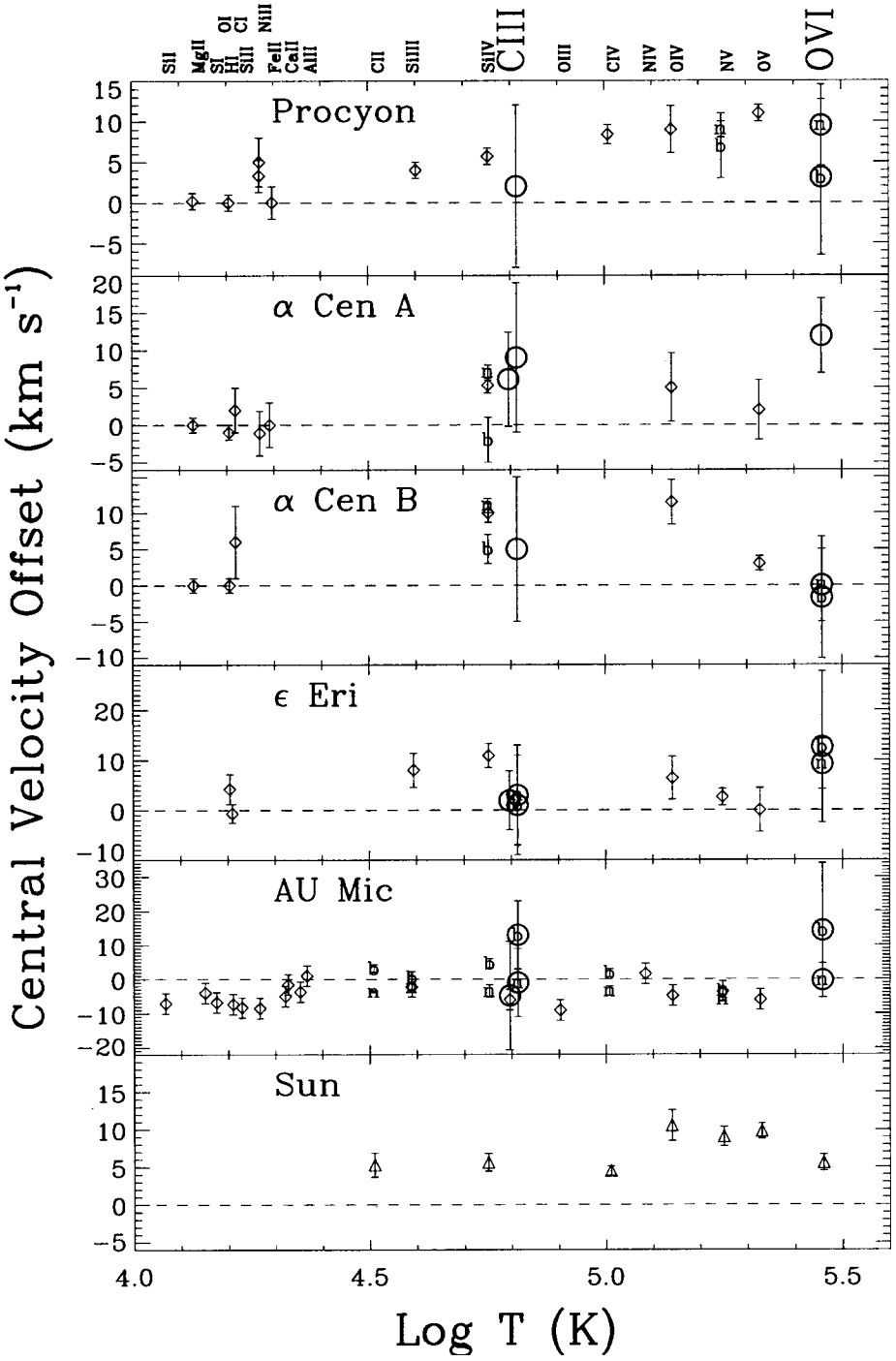

FIG. 14.—Line velocities for five of the stars observed by *FUSE*, and the Sun, as a function of formation temperature. AB Dor was not included because only a few emission lines have been observed. Open circles indicate *FUSE* observations of C III 977 Å, O VI 1032 and 1038 Å, and C III 1176 Å lines. *HST* observations are shown by diamonds. If two components were required to satisfactorily fit the line profile, they are indicated by "n" and "b," respectively. In some cases, the velocities of lines of the same species were averaged and represented by a single point. Dashed lines indicate the photospheric rest frame. The observed ions are labeled at the top of the plot.

AU Mic the broad component is consistently redshifted from the narrow component. A detailed discussion of the phenomenon, and the solar analog, can be found in Wood et al. (1997).

7. LINE PROFILES IN THE SPECTRUM OF ALTAIR

The hottest star in our survey, Altair (α Aqr = HD 187642; A7 V), is of particular interest because its shallow convective zone places it in the Herzsprung-Russell (H-R) diagram just where convection-powered dynamos first appear. Theoretical models predict that subsurface convective zones should decrease in thickness with increasing $T_{\rm eff}$ and disappear near $T_{\rm eff} \approx 8300$ K, corresponding to $B-V = 0.14$ (Bohn 1984; Ulmschneider et al. 1999). A subsurface convection zone is generally thought to be essential for the heating of the outer layers of late A and cooler stars, either by magnetic reconnection events (flares or micro-

flares), MHD wave dissipation, or acoustic wave shocks. For O and early B stars, X-ray emissions likely are not "coronal," but rather instabilities in radiatively driven winds (Lamers & Cassinelli 1999), and for the magnetic chemically peculiar B and early A stars a wind-fed magnetosphere model might be appropriate (Linsky, Drake, & Bastian 1992). Altair, along with other middle and late A stars, lies in the critical region in the H-R diagram where none of these mechanisms appear to operate.

Empirical tests for the presence of mechanical heating in the middle to late A stars, and the determination of which heating mechanism is dominant, are fraught with difficulties. X-ray emission, indicative of coronal plasma hotter than about 10^6 K, has been detected from a few A-type stars using *Einstein* (Schmitt et al. 1985) and the *Röntgen Satellite* (*ROSAT*) (Simon, Drake, & Kim 1995), but the identification of the emission with the A star is uncertain because of the competing hypothesis that the X-rays are emitted by a previously unknown late-type star companion. Probably the best case for an A-type star with a mechanically heated X-ray corona (not from a companion) is Altair, on the basis of its low coronal temperature (Schmitt et al. 1985), unlike the active late-type stars, and its bright ultraviolet emission lines.

Plasma at temperatures of 10^4–3×10^5 K radiates in ultraviolet emission lines. However, with increasing $T_{\rm eff}$, the background photospheric continuum becomes progressively brighter, making it difficult to detect emission lines. For A-type stars, this background rapidly decreases toward shorter wavelengths; thus, the most favorable opportunity for detecting emission lines from mechanically heated plasmas is at the shortest wavelengths in the ultraviolet. For example, the earliest type stars with detected emission in the C II 1335 Å, N V 1239 Å, and Lyα lines are Altair and α Cep, both A7 stars (Simon, Landsman, & Gilliland 1994; Walter, Matthews, & Linsky 1995; Simon & Landsman 1997). The A4 IV star τ^3 Eri shows the Si III 1206 Å line in emission (Simon & Landsman 1997). Prior to *FUSE*, the only instrument operating in the FUV that observed a late A–type star was *ORFEUS*, which detected the C III 977 and 1176 Å lines and the O VI 1032, and 1037 Å lines in α Cep with a resolution of $\sim$95 km s^{-1} (Simon & Ayres 1998). *FUSE* can build on this earlier study by observing these and other lines with a resolution of 20 km s^{-1}, sufficient to resolve the lines of rapidly rotating A-type stars.

The strong C II, C III, and O VI emission lines of Altair are depicted in Figures 8–10. The very broad profiles of these lines demonstrate that the rapidly rotating Altair, and not a more slowly rotating late-type companion, is responsible for the emission lines. The shape of the profiles of C III 977.02 Å, and the O VI 1031.93 and 1037.62 Å lines, is clearly not Gaussian, and their horned appearance suggests that they are optically thin lines that are rotationally broadened and limb brightened. We have therefore added to the figures the predicted shape of an optically thin emission line formed in a star with $v \sin i = 210$ km s^{-1} (van Belle et al. 2001) and smoothed by the instrumental line-spread function. The limb-brightened line profiles presented in Figures 8 and 9*a* are not unique solutions. One could produce other satisfactory fits by changing the limb-brightening function, the inclination of the star (which is poorly constrained; van Belle et al. 2001), or the altitude of the emitting region above the photosphere. However, two important points are clear from the line profiles of Altair. First, the horned appearance indicates that either there is significant brightening of emission toward the limb or the emitting region is preferentially located toward the equator (thereby reducing the area of the star with emission near zero velocity) rather than the poles. Doppler imaging of A stars, particularly chemically peculiar A stars with strong magnetic fields, have demonstrated that large-scale structures can exist on the surfaces of these stars (Rice 1996; Hatzes 1996). It is possible, therefore, that *FUSE* is Doppler imaging the stellar surface of Altair with observations of C III and O VI. If these line profiles are due to transient large-scale structures on the stellar surface, then we may expect the profile to change with time. The detailed analysis of these "horned" profiles will be the subject of a future paper. Second, the width of the lines require a $v \sin i \sim 210$ km s^{-1}, and do not show any indication of UV line narrowing produced by excess emission from the slowly rotating polar regions, as suggested by Simon et al. (1994).

8. THE FLARE SPECTRA OF AU MIC

The dMe dwarf stars exhibit many phenomena observed on the Sun, but with much larger energies. Their high stellar activity levels are demonstrated by frequent flares and strong magnetic fields (Saar 1994). Flares have been observed every time *HST* has pointed at AU Mic (Maran et al. 1994; Linsky & Wood 1994; Robinson et al. 2001). Pagano et al. (2000) discuss the quiescent spectrum, and Robinson et al. (2001) discuss the flare spectrum observed by STIS. Until this point in the paper we have dealt exclusively with the quiescent AU Mic spectrum, but we now turn our attention to the flare spectrum.

Since AU Mic was observed in time-tag mode, there is temporal information available for all photons with a temporal resolution of $\sim$1 s (Blair & Andersson 2001).[10] Figure 15 depicts a light curve in 10 s bins for four of the strongest emission lines in the *FUSE* spectrum and the continuum. The emission lines are presented in order of formation temperature, from the coolest (C II) to the hottest (O VI). Two flares are centered at 9.3 hr on 2000 August 26 and 10.6 hr on 2001 October 10, respectively, and both last $\sim$6 minutes. There is no significant time delay between any of the emission lines or the continuum. This is most obvious for the first flare because of its almost instantaneous rise phase in all emission features. Note the very different levels of response for the two flares. The O VI response is roughly equivalent in both flares, whereas the C III lines are much stronger in the first flare. There appears to be a preflare event before the first outburst, which is clearly evident in the C III lines, but not as obvious in the O VI or C II emission lines. The continuum count rate increases significantly in flare 1, but a continuum enhancement hardly registers during the second flare. Although the coronal Fe XVIII emission line is very weak, any enhancement during the flares would provide evidence for extremely high temperature components of the flare. We detect 11 and 12 Fe XVIII counts during flare 1 and flare 2, respectively. Based on quiescent levels adjacent to both flares, we expect 3.0 ± 0.6 and 5.6 ± 1.1 counts during these same times. Therefore, during the first flare there is a 2.3 σ detection of a enhancement, but only a 1.7 σ enhancement during the second flare. For comparison,

[10] The *FUSE* Observer's Guide Version 3.0 is available at: http://fuse.pha.jhu.edu/support/guide/guide.html.

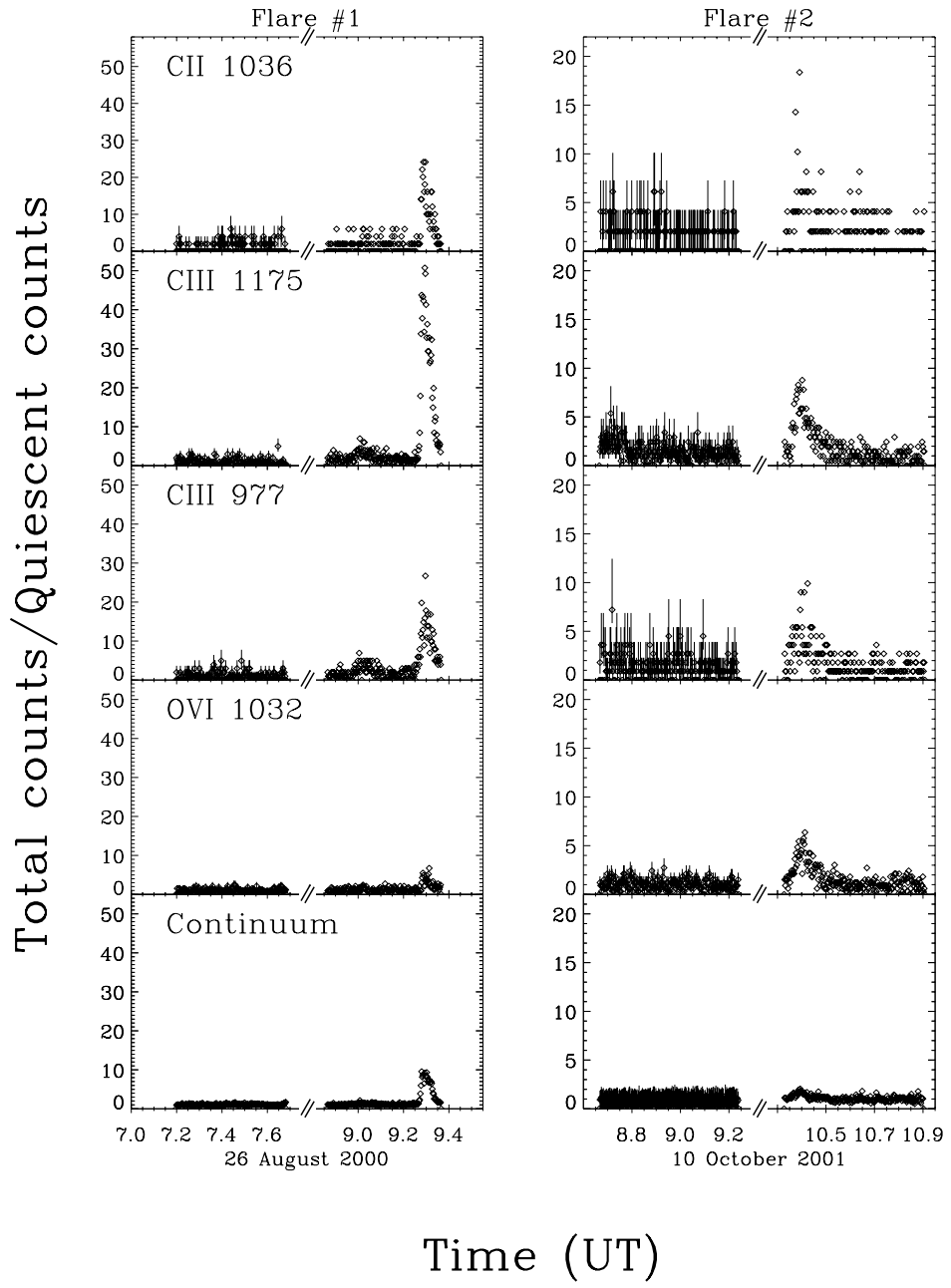

FIG. 15.—Time series of the C II 1036 Å, C III 977 Å, C III 1176 Å, and O VI 1032 Å emission lines, as well as the continuum for AU Mic. The first flare is at the end of the 2000 August 26 observation, and the second flare occurs near 10.4 hr on 2001 October 10. Error bars are displayed for the exposure preceding the flare only, but are typical for the entire observation. The line formation temperature increases from top to bottom. Note the preflare enhancement centered at 9.0 hr on 2000 August 26. Zero flux intervals indicate Earth occultations.

the weak increase in C II 1036 Å during the second flare is a 6.8 σ enhancement, while the detected increases for the rest of the emission lines shown in Figure 15 are $>10\,\sigma$.

The top panel of Figure 16 displays the continuum flux for each flare, obtained by integrating over $\sim$50 Å bins but deleting those wavelength regions that include obvious emission lines. (The shaded bars above the AU Mic spectrum in Figs. 1 and 2 indicate the line-free regions where the continuum was calculated.) Flare 1, in particular, exhibits increasing continuum flux toward shorter wavelengths. In theoretical models of the spectral energy distribution from hot optically thin plasmas, the dominant process producing continuum emission in the FUV is bremsstrahlung (Landini & Monsignori Fossi 1990). For temperatures $T > 10^5$ K, the continuum shape changes very little with temperature, and it always increases toward shorter wavelengths. Figure 16 compares the theoretical and observed flare continuum emission. The theoretical continuum intensity, calculated using the CHIANTI code version 3.03 (Dere et al. 1997, 2001), includes free-free and bound-free contributions. The thick dashed line is the simulated continuum emission at $\log T(\mathrm{K}) \sim 8.0$, in units of flux density per unit emission measure (ergs cm^{-2} s^{-1} Å^{-1} cm^5). Different assumptions regarding abundances and ionization equilibrium do not effect the shape of the theoretical continuum flux. The reference "quiescent" data refer to the same energy bandpasses

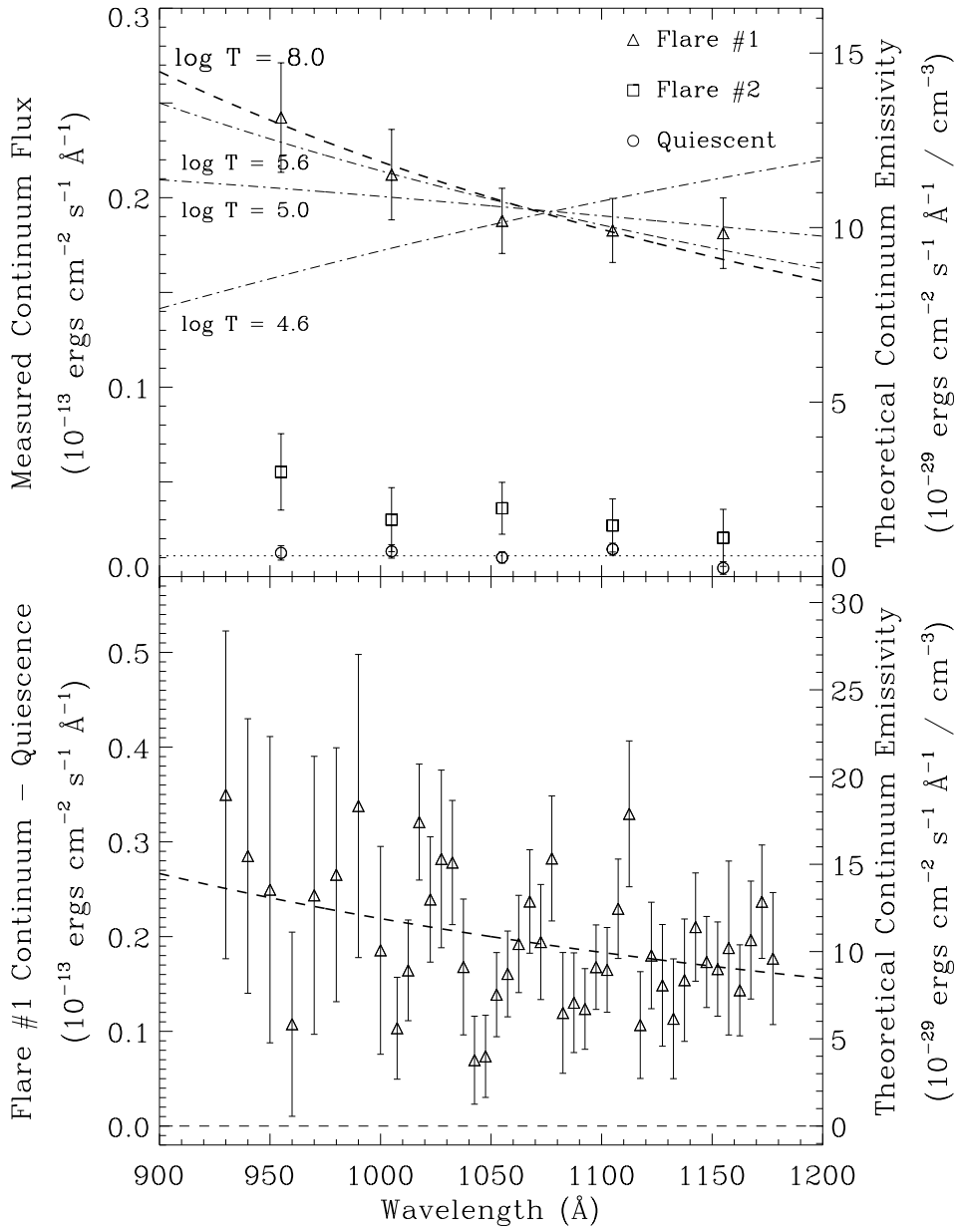

FIG. 16.—*Top*: Broadband (50 Å bins) continuum fluxes for the first AU Mic flare (2000 August 26; *triangles*) and second flare (2001 October 10; *squares*), compared with mean quiescent flux (*circles*). The dotted line indicates the mean value of the quiescent continuum. The bold dashed line indicates the predicted thermal bremsstrahlung continuum flux at $\log T(\mathrm{K}) \sim 8.0$ for the first flare (right axis). The dash-dotted lines are thermal bremsstrahlung continuum fits at various temperatures. The slope of thermal bremsstrahlung continuum starts to increase to shorter wavelength at $\log T(\mathrm{K}) \geq 5$, but it changes relatively little with increasing temperature. *Bottom*: Quiescent flux level subtracted from the flare 1 continuum flux, at the smallest possible bins. For the SiC channels (900–1000 Å), the bins are 10 Å, whereas for wavelengths above 1000 Å, the bins are 5 Å. The bold dashed line indicates the predicted thermal bremsstrahlung continuum flux at $\log T(\mathrm{K}) \sim 8.0$. In no bin does the flare continuum equal the quiescent level, as would be expected if we were observing numerous unresolved emission lines rather than a true continuum.

and were taken from the entire time interval outside the flares. The quiescent flux includes both stellar continuum (if present) and background, and is relatively constant over the entire *FUSE* bandpass. The dotted line indicates the mean continuum flux level during quiescence.

Robinson et al. (2001) discussed the possibility of detecting continuum emission at $\lambda > 1500$ Å during a flare on AU Mic with *HST*/STIS spectra. They attributed the observed rise in apparent continuum flux during a flare to be the result of enhanced emission in numerous weak lines, and thus not a true continuum. Their evidence is: (1) the continuum increase is gray over the range 1150–1720 Å, rather than increasing to shorter wavelengths; and (2) when the quiescent continuum is subtracted from the flare continuum, there are spectral regions that have zero flux. The stochastic nature of emission lines in wavelength space would tend to produce a jagged apparent continuum, but at wavelengths where there are no emission lines the flux levels should be the same as the quiescent flux levels seen by Robinson et al. (2001). *FUSE* is more likely to detect true continuum emission, if present, because the predicted flux increases toward shorter wavelengths. In Figure 16, the continuum emission observed by *FUSE* clearly does increase monotonically to shorter wavelengths across the

entire wavelength region. The bottom panel of Figure 16 demonstrates that even when we significantly reduce the bin size to 5–10 Å, and subtract off the quiescent emission, the flux level never reaches zero. Although the flux is noisy, it still rises smoothly toward shorter wavelengths. We conclude that the FUV continuum emission, particularly in the first flare, is a true continuum and not enhanced emission from numerous weak emission lines.

We tested the consistency of our thermal bremsstrahlung interpretation for the continuum by using CHIANTI to compute the emission measure and XSPEC to compute the X-ray luminosity of the flare based on the observed continuum flux for a range of temperatures. We used a one-temperature MEKAL model fit in XSPEC to calculate the X-ray flux in the *ROSAT* 0.1–2.4 keV band. The X-ray luminosity produced by a $\log T(\mathrm{K}) \sim 5.6$, 6.8, and 8.0 temperature flare would be $\log L_{\mathrm{X}}(\mathrm{ergs\ s^{-1}}) \sim 30.4$, 31.5, and 31.3, respectively, in this bandpass. Hünsch et al. (1999) obtained a quiescent X-ray luminosity for AU Mic of $\log L_{\mathrm{X}}$ (ergs $\mathrm{s^{-1}}$) ~ 29.7. The predicted *ROSAT* X-ray luminosity of our *FUSE* flare 1 is approximately 1–2 orders of magnitude greater than the quiescent luminosity. Tsikoudi & Kellett (2000) reported a factor of 10 increase in the *ROSAT* X-ray count rate over quiescent values during an impulsive flare on AU Mic, consistent with this prediction. Gagné et al. (1998) observed a factor of 20 increase in the *Rossi X-ray Timing Explorer* (*RXTE*) Proportional Counter Array (PCA) count rate during another flare on AU Mic.

Because the continuum shape is insensitive to temperature for $\log T(\mathrm{K}) > 5.5$, we attempted to constrain the temperature of the continuum plasma by calculating the emission measure of the hottest lines in the *FUSE* spectrum, O VI and Fe XVIII. In Table 11 we list the average line flux during the ~360 s duration of the flare, for the bright emission lines in the AU Mic spectrum that show significant changes during the flaring events. The quiescent levels were taken directly from Table 3. Only the strongest lines (C III and O VI) change dramatically in flare 2, whereas in flare 1 the fluxes of many emission lines increase. The average flare fluxes of O VI 1032 Å and Fe XVIII 975 Å were used to calculate an emission measure at their temperatures of maximum emissivity. The predicted thermal bremsstrahlung flux, based on the calculated emission measure for O VI, is a factor of 0.005 ± 0.006 times the observed continuum flux in flare 1 (more than 2 orders of magnitude too low), whereas the predicted continuum flux is only a factor of 0.42 ± 0.14 times the observed flux, based on the emission measure computed from the Fe XVIII flux. Therefore, we expect that the flaring plasma must cover a wide range of temperatures, including the range over which the ions shown in Figure 15 are abundant [$4.6 < \log T(\mathrm{K}) < 5.5$], as well as temperatures $\log T(\mathrm{K}) \gtrsim 5.8$, as demonstrated by the enhancement of Fe XVIII, and the presence of a strong continuum during flare 1. A formation temperature of $\log T(\mathrm{K}) = 7.5$ for Fe XVIII would bring the observed Fe XVIII flux and continuum flux shape into complete agreement. Detections of high-temperature ions, such as Fe XXIV, in observations of AU Mic with the *Extreme Ultraviolet Explorer* (*EUVE*) require material at such high temperatures (Monsignori Fossi et al. 1996). Gagné et al. (1998) used a two-temperature model to fit the flare spectra of AU Mic observed by *RXTE*, in which the temperature of the hot component was $\log T(\mathrm{K}) = 7.9$. High-temperature components are required to fit X-ray observations of many active M dwarfs (Pallavicini, Tagliaferri, & Stella 1990).

Figure 17 depicts profiles of the strongest lines during the AU Mic time series. The quiescent profiles are in the top row, and the profiles observed during the flares have had the quiescent contribution subtracted. Flare 1 displayed a strong increase in flux for these lines, with most of the flare emission redshifted. O VI has additional emission extending to $\sim +200$ km $\mathrm{s^{-1}}$, and the C III 1176 Å multiplet is highly blended, indicating that the individual emission lines are broader than during quiescence. The lines of the second flare are drastically different from the quiescent profiles. Conspicuous broad components are present, with FWHM $\gtrsim 175$ km $\mathrm{s^{-1}}$, with the flare contribution entirely in the broad component. The flaring plasma in the C III and O VI lines is downflowing during flare 1, but turbulent, with little or no net flow during flare 2.

As discussed in § 4.1, the $R_{\mathrm{C\,III}} \equiv \mathrm{C\ III}_{1176}/\mathrm{C\ III}_{977}$ flux ratio is sensitive to the electron density, but for active stars, the estimated electron density may not be physically significant. During the quiescent phase, we measured

TABLE 11
AU MIC EMISSION LINE FLUXES

Line	Wavelength (Å)	Integrated Flux (10^{-14} erg $\mathrm{cm^{-2}\ s^{-1}}$)		
		Quiescent	Flare 1	Flare 2
C III.....	977.02	15.3 ± 1.5	149 ± 16	69.1 ± 7.8
N III.....	989.80	1.2 ± 0.1	25.1 ± 6.0	<3.4
N III.....	991.51, 991.58	1.7 ± 0.2	43.3 ± 8.5	<3.3
O VI.....	1031.93	20.9 ± 2.4	43.7 ± 5.4	64.7 ± 6.5
C II.....	1036.34	0.7 ± 0.1	6.8 ± 2.0	<4.8
	1037.02	1.3 ± 0.1	17.0 ± 3.2	<5.9
O VI.....	1037.62	10.6 ± 1.1	21.9 ± 3.7	33.6 ± 3.6
S IV.....	1062.68	0.2 ± 0.1	10.5 ± 2.5	<1.9
	1073.00, 1073.53	< 0.2	18.6 ± 3.5	< 4.3
S III.....	1077.13	<0.2	7.9 ± 2.4	< 0.5
	1108.36	0.2 ± 0.1	9.3 ± 2.1	< 0.6
	1109.94, 1109.97	0.5 ± 0.1	12.5 ± 2.6	< 0.9
	1113.17, 1113.20, 1113.23	0.4 ± 0.1	13.0 ± 2.7	< 2.7
C III.....	1176.0	13.4 ± 1.3	320 ± 32	67.0 ± 6.7

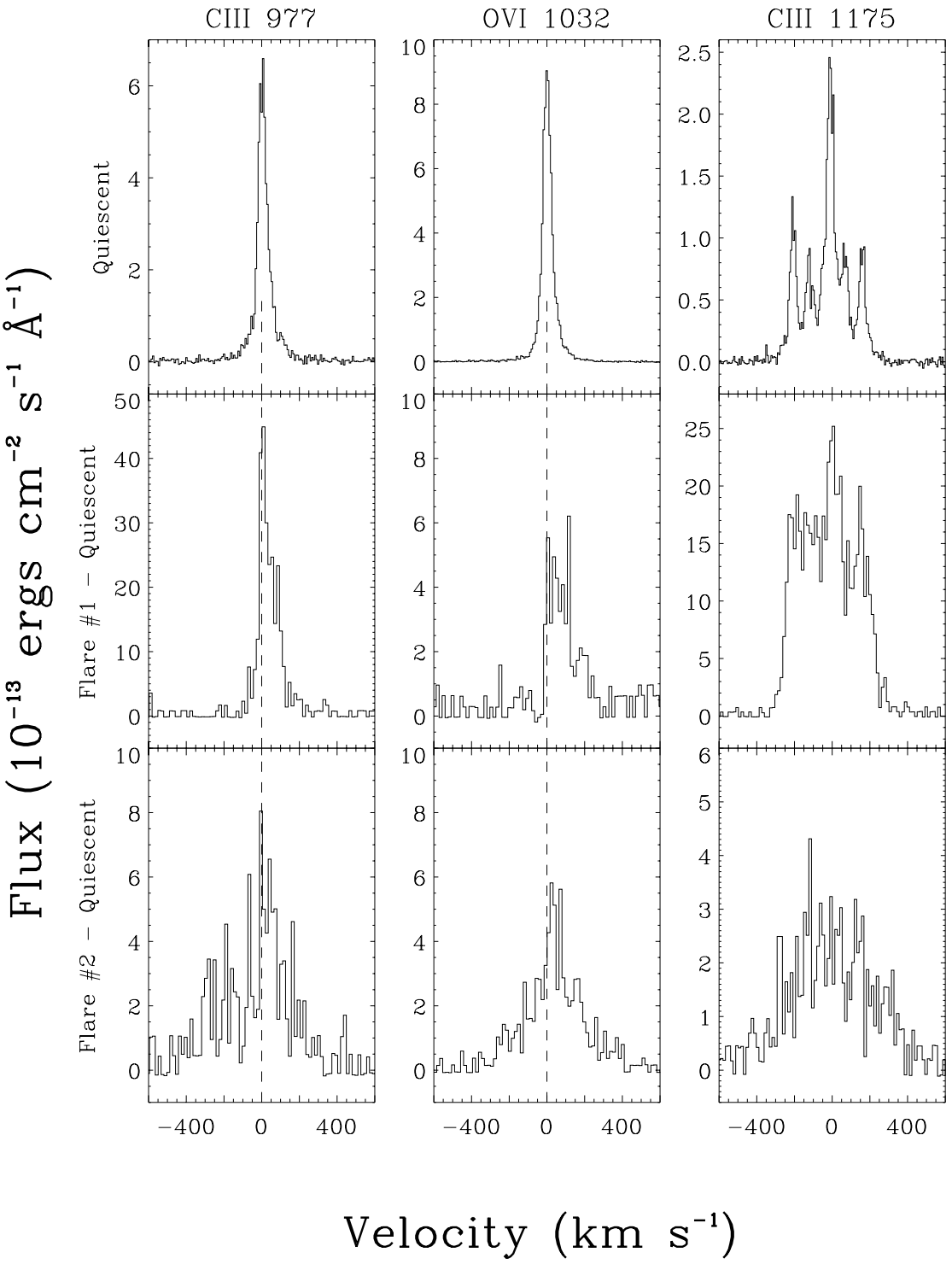

FIG. 17.—Profiles of the strongest lines in the *FUSE* spectrum of AU Mic in quiescence (*top*), during the first flare (*middle*), and second flare (*bottom*). Note the different line shapes for each flare. The quiescent contribution has been subtracted from the flare data.

$R_{\rm C\,III} = 0.88 \pm 0.12$, which is beyond the high electron density limit (see Table 6). For flare 1 $R_{\rm C\,III} = 2.15 \pm 0.32$, and for flare 2 $R_{\rm C\,III} = 0.97 \pm 0.15$ (see Table 11). The value for flare 1 is significantly higher than the quiescent value, suggesting densities even higher than the quiescent value. These high values demonstrate the difficulty of using the C III flux ratio to estimate accurate electron densities in active stars, where opacity and temperature effects conspire to prohibit the use of this diagnostic to calculate physically significant densities.

9. CONCLUSIONS

FUSE has provided high-quality 912–1180 Å spectra of seven dwarf stars: Altair (A7 IV), Procyon (F5 IV–V), α Cen A (G2 V), AB Dor (K1 V), α Cen B (K2 V), ϵ Eri

(K2 V), and AU Mic (M0 V). The spectra have a resolution $\lambda/\Delta\lambda \approx 20,000$ (15 km s^{-1}) and contain at least 40 identifiable emission lines or blends. These spectra have much higher S/N than previous FUV spectra of late-type stars obtained with the *Copernicus* and *ORFEUS* satellites. Analysis of the *FUSE* data yielded the following results:

1. These spectra display emission lines of ions abundant in the temperature range $\log T(\mathrm{K}) = 4.3$–5.5, including He II, C II, C III, N III, O IV, O VI, Ne V, Ne VI, Si IV, Si VI, S III, S IV, and S VI, as well as lower temperature chromospheric lines of H I (the Lyman series from Lyβ to at least Lyϵ), and C I. The spectra of α Cen A and B, ϵ Eri, and AU Mic (M0 V) also contain the 1–4 $Q(3)$ emission line of H_2 at 1163.9 Å, which is a fluorescent Werner band line pumped by the O VI 1031.8 Å emission line from the $v'' = 1$, $J'' = 3$ level in the H_2 ground electronic state. Another line, 1119.075 Å, produced by this fluorescent process is seen in AU Mic and ϵ Eri.

2. The highest temperature lines detected are Fe XIX 1118.06 Å and Fe XVIII 974.86 Å, coronal forbidden transitions formed at $\log T(\mathrm{K}) \approx 7.0$. These features are present in the most active dwarfs, ϵ Eri, AU Mic, and AB Dor.

3. We derived accurate absolute velocity scales for the eight spectral segments of the *FUSE* spectrograph using the interstellar C II 1036.3 Å and C III 977.0 Å absorption lines and the C III 1176 Å multiplet observed by STIS or GHRS. Since the *HST* spectrographs have very accurate velocity scales, the transfer of these velocity scales to *FUSE* spectra enables accurate measurements of the radial velocities of the brighter FUV emission lines. The O VI lines formed at $\log T(\mathrm{K}) = 5.5$ extend the pattern of increasing line centroid redshift indicative of downflows with line formation temperature best seen so far in the GHRS observations of Procyon for ions from Si III through O V. For α Cen A and AB Dor, the redshift of the O VI lines is also larger than for lines formed at lower temperatures, but in the cooler stars, the O VI redshifts are close to zero. The dependence of line centroid velocity on temperature provides information on global flow patterns in the inhomogeneous transition region plasmas. Redshifts of optically thin lines indicate that downflowing plasma has higher emission measure at that temperature than the upflowing plasma.

4. Comparison of the *FUSE* C III and O VI fluxes with *ORFEUS* and GHRS and STIS (C III 1176 Å multiplet only) reveal an interesting test of the photometric accuracy of *FUSE*. For those stars observed by *FUSE* through the LWRS (e.g., AB Dor and AU Mic), the agreement with previous measurements is quite good (differences of less than 14%) despite the intrinsic variability of the stars. On the other hand, those stars observed by *FUSE* through the MDRS (e.g., Procyon, α Cen A and B, and ϵ Eri), show much poorer agreement, with differences as large as 52%. The likely reason is that stars tend to drift out of the MDRS for all spectral segments except LiF1A, which is used for guiding. Since the loss of flux is difficult to identify until the star is almost completely outside of the aperture, the absolute fluxes of stars observed through the MDRS should be considered uncertain.

5. The emission-line profiles in many cases could be modeled by a double Gaussians consisting of narrow and broad components. We interpret the broad components as evidence for explosive nonthermal motions caused by magnetic reconnection events (e.g., "microflares") and/or as a signature of transition region emission near the footpoints of large coronal loops. There is a trend of increasing relative importance of the broad components with increasing coronal activity as indicated by the proxies, C IV and X-rays, suggesting that heating by these mechanisms is increasingly important in the active stars. There is also a trend of decreasing relative importance of the broad components with increasing line formation temperature, implying that the spectroscopic impact of microflare heating might be more important in the lower transition region than at $\log T(\mathrm{K}) = 5.5$, where the O VI lines are formed.

6. The nonthermal velocities inferred from the narrow components of the C III and O VI lines show a trend of increasing velocity with decreasing surface gravity. The nonthermal velocities inferred from the broad components show no obvious trend with surface gravity.

7. The O VI and C III lines of the hottest star in our sample, Altair (A7 IV), show broad horned features that can be modeled as optically thin limb-brightened rotationally broadened profiles. The line shapes are inconsistent with formation in a late-type star, confirming that the transition region emissions, and by implication the coronal X-rays, are from the A7 star itself.

8. The C III 1176 Å to C III 977 Å flux ratio can be used to gauge electron densities. The *FUSE* observations of α Cen A and B indicate $\log n_e \approx 9.6$ at $\log T(\mathrm{K}) = 4.8$. For the more active stars, the electron densities are substantially larger, but the uncertainties are amplified because the ratios are near the high-density limit.

9. *FUSE* caught two flares on AU Mic, indicated by enhanced emission line fluxes. The first flare also showed a continuum increasing to shorter wavelengths, which we modeled as free-free emission from a hot plasma, $\log T(\mathrm{K}) \geq 5.6$. The C III and O VI profiles from the first flare show enhanced redshifted emission out to +200 km s^{-1}, while those from the second flare display enhanced broad wings but no Doppler shifts.

This work is based on data obtained for the Guaranteed Time Team by the NASA-CNES-CSA *FUSE* mission, which is operated by The Johns Hopkins University. Financial support to US participants has been provided by NASA contract NAS5-32985. This research has made use of the SIMBAD database, operated at CDS, Strasbourg, France. We thank Greg Herczeg and Graham Harper for discussions of H_2 fluorescence.

APPENDIX

ESTABLISHING THE ABSOLUTE VELOCITY SCALE

The *FUSE* spectrograph has four separate optical paths: two have LiF overcoated optics channels (LiF1 and LiF2) for high effective area at the longer wavelengths, and two have SiC optics channels (SiC1 and SiC2) for the largest feasible effective area below 1000 Å. Each of these four channels has two adjacent detectors (A and B) that cover the wavelength interval of the

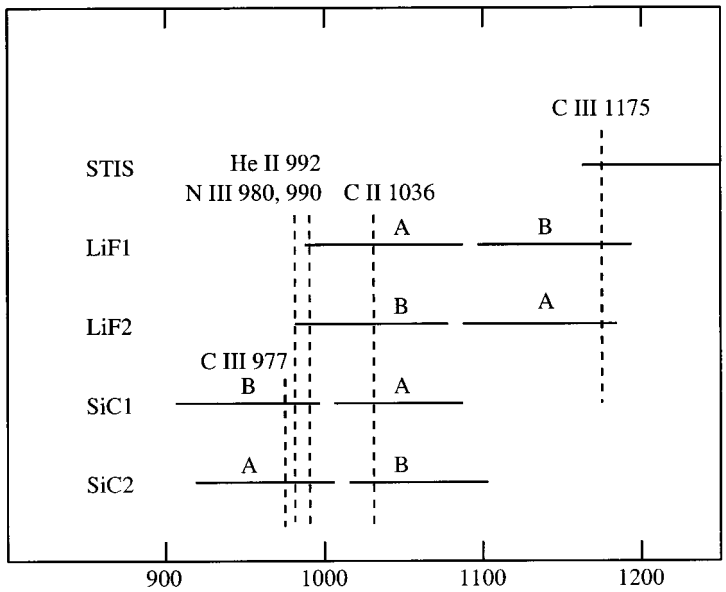

FIG. 18.—Wavelength intervals observed with the eight *FUSE* segments and STIS. Dashed lines indicate transitions used to cross-calibrate the wavelength scales.

channel with a small gap between them. Thus the data consist of eight spectral segments (i.e., LiF1A, LiF1B, . . ., SiC2B), with considerable wavelength overlap among the segments, as depicted in Figure 18.

CalFUSE version 2.0.5 provides a relative wavelength scale accurate to about ± 5 km s^{-1} within each of the eight data segments. The absolute wavelength scale for each segment requires knowledge of the star's position in the aperture as a function of time for each of the four optical paths, and any thermal drifts within each segment. Unfortunately, this information is not available empirically, so we must calibrate the wavelength scale of each segment using observed spectral features from other measurements having an absolute velocity reference. For this purpose we use the interstellar C II 1036.3367 Å absorption line (Fig. 19) seen in all of the stars, and the C III 977.020 Å interstellar line (Fig. 8) found only in AB Dor. These features are in absorption against the stellar C II and C III emission lines. Based on photoionization models of the LISM (Slavin & Frisch 2002) and recent observations (Wood et al. 2002b), 1%–4% of carbon in the warm partially ionized LISM will be in the form of C III, while at least 95% is in the form of C II. Because C III will coexist with C II and Mg II in the same parcel of material, they should have the same bulk motion, and their absorption lines should be observed with identical projected velocities. Table 1 includes the known heliocentric velocities of interstellar absorption for the lines of sight to the targets. In those cases where several velocity components are known, we have constrained the velocity separation, and ratio of column densities, to be identical with high-resolution GHRS or STIS observations of the Mg II *h* and *k* lines or C II 1334.532 Å line. Since the relatively low spectral resolution of *FUSE* does not provide any information on the Doppler parameter for the interstellar lines, we constrain the Doppler parameters to a range typical of the warm LISM.

The C II 1036.3367 Å line is present in four spectral segments (LiF1A, LiF2B, SiC1A, and SiC2B), as shown in Figure 18, but has the highest S/N in the most sensitive channel LiF1A. For each star we compared the observed LiF1A profile of the C II 1036.3367 Å line with the other member of the multiplet, C II 1037.0182 Å, on the velocity scale provided by CalFUSE. Both C II lines are present alongside the O VI 1037.6167 Å line in Figures 9*a* and 6*b*. Because the lower state of the C II 1037.0182 Å line is 64 cm^{-1} above the ground state, we do not expect to see a LISM absorption component. The flux ratio of the 1037/1036 lines is 2.0 in the optically thin limit, but can decrease to 1.0 when the lines become optically thick. For each target, interstellar absorption is clearly present in the 1036.3367 Å line (see Fig. 19) but not the 1037.0182 Å line. We reconstruct the C II 1036.3367 Å profile using the unabsorbed C II 1037.0182 Å line. For most targets the O VI 1037.6167 Å line is narrow and does not blend with the C II features. In the fastest rotating stars (Altair and AB Dor), the wings of O VI do heavily obscure the C II lines, but they also provide a smooth and simple continuum with which to measure the LISM absorption. We then fit the proper number of ISM components derived from high-resolution Mg II observations of these stars from *HST*. In three cases, multiple components are known to exist along the sight line. In order to limit the number of free parameters, we fixed the velocity difference between the interstellar components, the column density ratio among them, and the Doppler width parameter based on analyses of the resolved Mg II lines. Ultimately, the only free parameters in the ISM fitting are (1) the total column density of C II ISM material, often with large errors due to the low spectral resolution and our incomplete knowledge of the temperature of the clouds; and, most importantly, (2) the central velocity of one of the components, before convolution with the line-spread function, which provides us with an accurate absolute wavelength calibration. For three stars, α Cen A, ϵ Eri, and AU Mic, we have high-resolution spectra of the C II 1334.532 Å LISM line, which provides an accurate measurement of the C II column density. For these cases, the only free parameter in the ISM fit to the C II 1036.3367 Å line is the central velocity of the interstellar absorption. The dotted lines in Figure 19 indicate the centroid of the interstellar absorption based on GHRS or STIS measurements of the Mg II and Fe II lines, which should provide an absolute heliocentric velocity accurate to ± 5 km s^{-1} (Redfield & Linsky 2002b). For four of the seven stars, the *FUSE* and *HST* velocity scales are in good agreement (within about 6 km s^{-1}). For both AB Dor and ϵ Eri, however, the *FUSE* LiF1A velocity scale is offset by more than 15 km s^{-1}

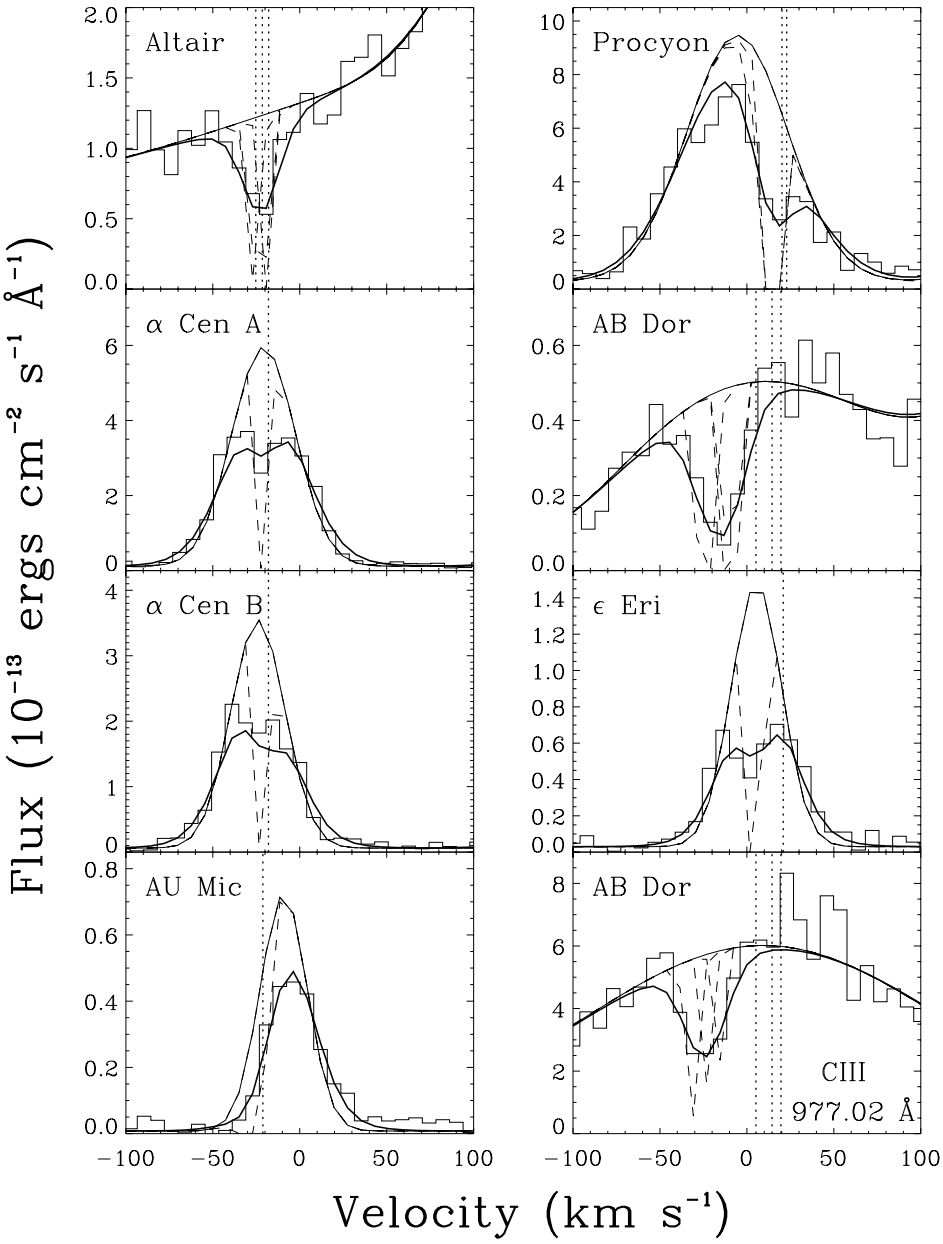

FIG. 19.—C II 1036.3367 Å interstellar line, used as an absolute wavelength reference, illustrated as a histogram on a heliocentric velocity scale. Thin solid lines indicate adopted intrinsic stellar line profiles. The ISM absorption is represented by dashed lines. Thick solid lines indicate the final fits, including instrumental broadening. Vertical dotted lines mark the predicted LISM velocities based on high-resolution *HST* data. A fit to C III 977.0201 Å in AB Dor is displayed in the lower right panel.

with respect to *HST*. AB Dor was observed early in the mission, when the *FUSE* spectrograph was not well understood. The large correction for ϵ Eri indicates that the star probably was not well centered in the aperture. The C III 977.020 Å line in AB Dor also shows an interstellar feature (Fig. 19, *lower right panel*), which we use to correct the SiC2A channel. Table 12 lists the velocity corrections to place the LiF1A and SiC2A channels on an absolute heliocentric velocity scale consistent with the interstellar line radial velocities measured by *HST*.

The brightest stellar emission feature in the LiF1A bandpass is O VI 1031.925 Å. Since it is present in three other segments (LiF2B, SiC1A, and SiC2B), we adopted O VI as the velocity fiducial to correct the wavelength scales of these segments. We were able to calibrate the SiC1B and SiC2A segments by comparing features in the overlap region (987–1006 Å) with LiF1A: N III 989.799 Å, blended 991.511 Å and 991.577 Å, and He II 992.363 Å. The locations of these lines are far enough from the edge of the detectors that the edge distortions are still $\lesssim$10 pixels and are well characterized by the CalFUSE wavelength calibration routine. Unfortunately, there are no strong emission lines in the overlap region (1087–1103 Å) for the two remaining detector segments, LiF1B and LiF2A. For five of the seven stars, however, we are able to calibrate the absolute wavelength scales for these channels by comparing the C III 1176 Å multiplet in the *FUSE* spectra with GHRS and STIS spectra (which are calibrated by an on-board lamp). The wavelength offsets based on *HST* are listed in Table 5. *HST* observations of Altair and AB Dor were obtained with $\sim$10 times lower spectral resolution than *FUSE*, and therefore cannot help with the absolute wavelength scale. However, they do provide a useful integrated flux of the C III 1176 Å multiplet for comparison.

TABLE 12

WAVELENGTH OFFSETS BASED ON ISM MEASUREMENTS AND COMPARISON WITH *HST* OBSERVATIONS

Star Name	C III (977 Å) Offset (km s^{-1}) SiC 2A	C II (1036 Å) Offset (km s^{-1}) LiF 1A	C III (1176 Å) Offset (km s^{-1}) LiF 2A
Altair	...	+1.6	−2[a]
Procyon	...	+6.1	...
α Cen A.....	...	+2.9	−6.7
AB Dor	+36.5	+27.5	+5[a]
α Cen B.....	...	+2.1	...
ϵ Eri	...	+17.7	+0.0
AU Mic.....	...	+9.6	+11.7

[a] Low-resolution *HST* comparison spectra; velocity correction accurate to ±40 km s^{-1}.

REFERENCES

Ake, T. B., Dupree, A. K., Young, P. R., Linsky, J. L., Malina, R. F., Griffiths, N. W., Siegmund, O. H. W., & Woodgate, B. E. 2000, ApJ, 538, L87

Ake, T. B., et al. 2001, in Twelfth Cambridge Workshop on Cool Stars, Stellar Systems and the Sun (Cambridge: SAO), in press

Ayres, T. R., & Linsky, J. L. 1980, ApJ, 241, 279

Ayres, T. R., Stencel, R. E., Linsky, J. L., Simon, T., Jordan, C., Brown, A., & Engvold, O. 1983, ApJ, 274, 801

Bevington, P. R., & Robinson, D. K. 1992, Data Reduction and Error Analysis for the Physical Sciences (New York: McGraw-Hill)

Blair, B., & Andersson, B.-G. 2001, The *FUSE* Observer's Guide Version 3.0 (Baltimore: Johns Hopkins Univ.)

Bohn, H. U. 1984, A&A, 136, 338

Brandt, J. C., et al. 2001, AJ, 121, 2173

Brekke, P. 2000, Sol. Phys., 190, 379

Brown, A., Jordan, C., Stencel, R. E., Linsky, J. L., & Ayres, T. R. 1984, ApJ, 283, 731

Curdt, W., Brekke, P., Feldman, U., Wilhelm, K., Dwivendi, B. N., Schühle, U., & Lemaire, P. 2001, A&A, 375, 591

Curdt, W., et al. 1997, A&AS, 126, 281

Del Zanna, G., Landini, M., & Mason, H. E. 2002, A&A, 385, 968

Dere, K. P., Bartoe, J.-D. F., & Brueckner, G. E. 1989, Sol. Phys., 123, 41

Dere, K. P., Landi, E., Mason, H. E., Monsignori Fossi, B. C., & Young, P. R. 1997, A&AS, 125, 149

Dere, K. P., Landi, E., Young, P. R., & Del Zanna, G. 2001, ApJS, 134, 331

Dixon, V. 2001, Introduction to CalFUSE Version 2.0 (Baltimore: Johns Hopkins Univ.)

Doschek, G. A., Feldman, U., & Bohlin, J. D. 1976, ApJ, 205, L177

Dring, A. R., Linsky, J., Murthy, J., Henry, R. C., Moos, W., Vidal-Madjar, A., Audouze, J., & Landsman, W. 1997, ApJ, 488, 760

Evans, R. G., Jordan, C., & Wilson, R. 1975, MNRAS, 172, 585

Fekel, F. C. 1997, PASP, 109, 514

Feldman, P. D., Sahnow, D. J., Kruk, J. W., Murphy, E. M., & Moos, H. W. 2001, J. Geophys. Res., 106, 8119

Feldman, U., & Doschek, G. A. 1991, ApJS, 75, 925

Gagné, M., Valenti, J., Johns-Krull, C., Linsky, J., Brown, A., & Güdel, M. 1998, in ASP Conf. Ser. 154, The Tenth Cambridge Workshop on Cool Stars, Stellar Systems and the Sun, ed. R. A. Donahue & J. A. Bookbinder (San Francisco: ASP), 1484

Hale, A. 1994, AJ, 107, 306

Harper, G. M., Wilkinson, E., Brown, A., Jordan, C., & Linsky, J. L. 2001, ApJ, 551, 486

Hatzes, A. P. 1996, in IAU Symp. 176, Stellar Surface Structure, ed. K. G. Strassmeier & J. L. Linsky (Dordrecht: Kluwer), 305

Hünsch, M., Schmitt, J. H. M. M., Sterzik, M. F., & Voges, W. 1999, A&AS, 135, 319

Hurwitz, M., et al. 1998, ApJ, 500, L1

Jordan, C., Ayres, T. R., Brown, A., Linsky, J. L., & Simon, T. 1987, MNRAS, 225, 903

Jordan, C., Sim S. A., McMurry, A. D., & Aruvel, M. 2001, MNRAS, 326, 303

Lallement, R., Ferlet, R., Lagrange, A. M., & Vidal-Madjar, A. 1995, A&A, 304, 461

Lamers, J. G. L. M. & Cassinelli, J. P. 1999, Introduction to Stellar Winds (Cambridge: Cambridge Univ. Press)

Landini, M. & Monsignori Fossi, B. C. 1990, A&AS, 82, 229

Linsky, J. L., Diplas, A., Wood, B. E., Brown, A., Ayres, T. R., & Savage, B. D. 1995, ApJ, 451, 335

Linsky, J. L., Drake, S. A., & Bastian, T. S. 1992, ApJ, 393, 341

Linsky, J. L. & Wood, B. E. 1994, ApJ, 430, 342

Linsky, J. L. & Wood, B. E. 1996, ApJ, 463, 254

Maran, S. P., et al. 1994, ApJ, 421, 800

Mazzotta, P., Mazzitelli, G., Colafrancesco, S., & Vittorio, N. 1998, A&AS, 133, 403

Monsignori Fossi, B. C., Landini, M., Del Zanna, G., & Bowyer, S. 1996, ApJ, 466, 427

Moos, H. W., et al. 2000, ApJ, 538, L1

Oegerle, B., Murphy, E., & Kriss, J. 2000, The *FUSE* Data Handbook Version 1.1 (Baltimore: Johns Hopkins Univ.)

Pagano, I., Linsky, J. L., Carkner, L., Robinson, R. D., Woodgate, B., & Timothy, G. 2000, ApJ, 532, 497

Pallavicini, R., Golub, L., Rosner, R., Vaiana, G. S., Ayres, T., & Linsky, J. L. 1981, ApJ, 248, 279

Pallavicini, R., Tagliaferri, G., & Stella, L. 1990, A&A, 228, 403

Peter, H. 2000, A&A, 360, 761

———. 2001, A&A, 374, 1108

Peter, H., & Judge, P. G. 1999, ApJ, 522, 1148

Pettersen, B. R. 1980, A&A, 82, 53

Redfield, S., Ayres, T. R., Linsky, J. L., Ake, T. B., Robinson, R. D., Dupree, A. K., & Young, P. R. 2002a, ApJ, submitted

Redfield, S., & Linsky, J. L. 2002b, ApJS, 139, 439

Rice, J. B. 1996, in IAU Symp. 176, Stellar Surface Structure, ed. K. G. Strassmeier & J. L. Linsky (Dordrecht: Kluwer), 19

Robinson, R. D., Linsky, J. L., Woodgate, B. E., & Timothy, J. G. 2001, ApJ, 554, 368

Saar, S. H. 1994, in IAU Symp. 154, Infrared Solar Physics, ed. D. M. Raban, J. T. Jeffries, & C. Lindsey (Dordrecht: Kluwer), 437

Sahnow, D. J., et al. 2000, ApJ, 538, L7

Schmitt, J. H. M. M., Cutispoto, G., & Krautter, J. 1998, ApJ, 500, L25

Schmitt, J. H. M. M., Golub, L., Harnden, F.R., Jr., Maxson, C. W., Rosner, R., & Vaiana, G. S. 1985, ApJ, 290, 307

Schmitt, J. H. M. M., et al. 1997, A&A, 325, 249

Simon, T., & Ayres, T. R. 1998, ApJ, 500, L37

Simon, T., & Drake, S. A. 1989, ApJ, 346, 303

Simon, T., Drake, S. A., & Kim, P. D. 1995, PASP, 107, 1034

Simon, T., & Landsman, W. B. 1997, ApJ, 483, 435

Simon, T., Landsman, W. B., & Gilliland, R. L. 1994, ApJ, 428, 319

Slavin, J. D., & Frisch, P. C. 2002, ApJ, 565, 364

Smith, G., Edvardsson, B., & Frisk, U. 1986, A&A, 165, 126

Smith, M. A. 1978, ApJ, 224, 584

Tsikoudi, V., & Kellett, B. J. 2000, MNRAS, 319, 1147

Ulmschneider, P., Theurer, J., Musielak, Z. E., & Kurucz, R. 1999, A&A, 347, 243

van Belle, G. T., Ciardi, D. R., Thompson, R. R., Akeson, R. L., & Lada, E. A. 2001, ApJ, 559, 1155

Vilhu, O., Muhli, P., Huovelin, J., Hakala, P., Rucinski, S. M., & Collier Cameron, A. 1998, AJ, 115, 1610

Walter, F. W., Matthews, L. D., & Linsky, J. L. 1995, ApJ, 447, 353

Wilkinson, E., Harper, G. M., Brown, A., & Herczeg, G. K. 2002, AJ, submitted

Wood, B. E., Harper, G. M., Linsky, J. L., & Dempsey, R. C. 1996, ApJ, 458, 761

Wood, B. E., Linsky, J. L., & Ayres, T. R. 1997, ApJ, 478, 745

Wood, B. E., Linsky, J. L., Hébrard, G., Vidal-Madjar, A., Lemoine, M., Moos, H. W., Sembach, K. R., & Jenkins, E. B. 2002a, ApJS, 140, 91

Wood, B. E., Redfield, S., Linsky, J. L., & Sahu, M. S. 2002b, ApJ, submitted

Young, P. R., Dupree, A. K., Wood, B. E., Redfield, S., Linsky, J. L., Ake, T. B., & Moos, H. W. 2001, ApJ, 555, L121